REYNOLDS NUMBER EXTRAPOLATION FOR WIND TURBINE AIRFOIL POLARS: A DATA-DRIVEN APPROACH

A THESIS SUBMITTED TO
THE GRADUATE SCHOOL OF NATURAL AND APPLIED SCIENCES
OF
MIDDLE EAST TECHNICAL UNIVERSITY

BY

AHMET CAN ÖZGÖREN

IN PARTIAL FULFILLMENT OF THE REQUIREMENTS
FOR
THE DEGREE OF MASTER OF SCIENCE
IN
AEROSPACE ENGINEERING

JANUARY 2023

Approval of the thesis:

REYNOLDS NUMBER EXTRAPOLATION FOR WIND TURBINE AIRFOIL POLARS: A DATA-DRIVEN APPROACH

submitted by **AHMET CAN ÖZGÖREN** in partial fulfillment of the requirements for the degree of **Master of Science** i**n Aerospace Engineering, Middle East Technical University** by,

Prof. Dr. Halil Kalıpçılar
Dean, Graduate School of **Natural and Applied Sciences** _____

Prof. Dr. Serkan Özgen
Head of the Department, **Aerospace Engineering** _____

Prof. Dr. Oğuz Uzol
Supervisor, **Aerospace Engineering, METU** _____

Examining Committee Members:

Prof. Dr. Serkan Özgen
Aerospace Eng., METU _____

Prof. Dr. Oğuz Uzol
Aerospace Eng., METU _____

Asst. Prof. Dr. Mustafa Perçin
Aerospace Eng., METU _____

Assoc. Prof. Dr. Elif Oğuz
Civil Eng., METU _____

Asst. Prof. Dr. Onur Baş
Mechanical Eng., TEDU _____

Date: 19.01.2023

I hereby declare that all information in this document has been obtained and presented in accordance with academic rules and ethical conduct. I also declare that, as required by these rules and conduct, I have fully cited and referenced all material and results that are not original to this work.

Name Last name : Ahmet Can Özgören

Signature :

ABSTRACT

REYNOLDS NUMBER EXTRAPOLATION FOR WIND TURBINE AIRFOIL POLARS: A DATA-DRIVEN APPROACH

Özgören, Ahmet Can
Master of Science, Aerospace Engineering
Supervisor : Prof. Dr. Oğuz Uzol

January 2023, 87 pages

In this thesis, a data-driven methodology based on power law is proposed to extrapolate the Reynolds number, and its prediction performance for wind turbine airfoil aerodynamic polars are investigated. For this purpose, a database is constructed from experimentally obtained aerodynamic data from open literature for airfoils with thickness-to-chord ratio (t/c) values in the range of 15% to 30%, which are more relevant to wind turbine blade design applications. The airfoils included in the database are inversely parameterized using the PARSEC airfoil parameterization method to enhance the database numerically in terms of the geometrical properties. Then, Pareto analysis is performed to understand the sensitivity of maximum lift coefficient ($C_{l\,max}$) and minimum drag coefficient ($C_{d\,min}$) variations to PARSEC geometrical properties as well as the Reynolds number using JMP statistical software. Based on this analysis, response surfaces are generated to predict $C_{l\,max}$ and $C_{d\,min}$ of a given airfoil operating at a given Reynolds number. These predicted values are then utilized in a proposed power law based estimation methodology to obtain predictions for the full polars. This proposed method is tested by making predictions for airfoils divided into two groups: those that are included in the

database and those that are not. At last, predicted aerodynamic polars for the FFA-W3-241 airfoil are implemented in aeroelastic BEM simulations to investigate their effects on the operation of the DTU 10 MW reference wind turbine.

Keywords: Reynolds Number Extrapolation, Wind Turbine Airfoils, Aerodynamic Polars

ÖZ

RÜZGAR TÜRBİNİ KANAT PROFİLİ KUTUPLARI İÇİN REYNOLDS SAYISI DIŞDEĞERLEMESİ: VERİ DAYALI YAKLAŞIM

Özgören, Ahmet Can
Yüksek Lisans, Havacılık ve Uzay Mühendisliği
Tez Yöneticisi: Prof. Dr. Oğuz Uzol

Ocak 2023, 87 sayfa

Bu tezde, Reynolds sayısını dışdeğerlemek için kuvvet yasasına dayanan veriye dayalı bir yöntem önerilmiş ve önerilen bu yöntemin rüzgar türbini kanat profili kutupları için tahmin performansı incelenmiştir. Bu amaç doğrultusunda, rüzgar türbini kanat tasarımı uygulamalarına daha uygun olması için, kalınlık-kiriş oranı (t/c) %15 ila %30 aralığında olan kanat profilleri için açık literatürden deneysel olarak elde edilen aerodinamik verileri içeren bir veritabanı oluşturulmuştur. Veritabanına dahil edilen tüm kanat profilleri, veritabanını geometrik özellikler açısından sayısal olarak zenginleştirmek için PARSEC kanat profili parametreleştirme yöntemi kullanılarak parametrelendirilmiştir. Ardından, maksimum kaldırma katsayısı ($C_{l\,max}$) ve minimum sürükleme katsayısı ($C_{d\,min}$) varyasyonlarının, PARSEC geometrik özelliklerine ve ayrıca Reynolds sayısına duyarlılığını anlamak için JMP istatistik yazılımı kullanılarak bir Pareto analizi yapılmıştır. Bu analize dayalı olarak, belirli bir Reynolds sayısında çalışan bir kanat profilinin $C_{l\,max}$ ve $C_{d\,min}$ değerlerini tahmin etmek için tepki yüzeyi oluşturulmuştur. Bu tahmin edilen değerler daha sonra, kutupların tamamını tahmin etmek için önerilen bir kuvvet yasasına dayalı tahmin yönteminde kullanılmaktadır.

Önerilen bu yöntem, veri tabanına dahil olan ve olmayan olarak iki gruba ayrılan kanat profilleri için tahminler yapılarak test edilmiştir. Son olarak, FFA-W3-241 kanat profili için tahmin edilen aerodinamik kutuplar, DTU 10 MW referans rüzgar türbininin çalışmasını nasıl etkilediklerini görmek için aeroelastik BEM simülasyonlarına uygulanmıştır.

Anahtar Kelimeler: Reynolds Sayısı Dışdeğerlemesi, Rüzgar Türbini Kanat Profili, Aerodinamik Kutuplar

"Bir çift mavi gözün ışığında…

Her şey çok güzel olacak!”

ACKNOWLEDGEMENTS

Firstly, I would like to express my gratitude to my supervisor, Prof. Dr. Oğuz Uzol, for his support, guidance and valuable insights throughout my research. I am honored to have been his graduate student and grateful for the opportunity to learn from him. His guidance greatly influenced my growth as a researcher and professional. I am particularly grateful for his availability and support.

I would like to thank all my thesis committee members, Prof. Dr. Serkan Özgen, Asst. Prof. Dr. Mustafa Perçin, Assoc. Prof. Dr. Elif Oğuz and Asst. Prof. Dr. Onur Baş.

I would like to express my gratitude to DTU Wind Energy for providing me with the licenses of HAWC2 Software, free of charge, to conduct aeroelastic BEM simulations.

Also, I would also like to thank the authors of CB2: Airfoil Optimization with GUI tool for providing me with the inverse PARSEC airfoil parameterization code. Their code has been an essential part of my research.

I would like to express my gratitude to committee members of the 14th European Fluid Mechanics Conference for providing me with the opportunity to present a portion of this thesis study. Their platform has been a great opportunity for me to share my research and receive valuable feedback from experts in the field.

Also, I would like to express my appreciation to HAVELSAN Inc. for their support and encouragement throughout this study. I would also like to extend my thanks to my colleagues for their support and guidance.

I would like to thank my friends Abdullah Tan, Ahmet Çakır, Buğrahan Öztürk, Burak Daldal, Emre Avşar and Mustafa Yiğithan Başer for their endless support.

I would also like to extend a very special thank you to my love, İrem İskender, for her unwavering support and presence throughout my graduate life. Her understanding, patience and encouragement were essential in helping me to complete this research and I am deeply grateful for her love and support.

Lastly, I would like to express my eternal gratitude to my parents, Nevin-İlhami Özgören and Betül-Mete Özgören, for their unwavering love and support throughout my life. And also my nephew Derin Alya, who was always there to make me happy and bring a smile on my face during the difficult times of my research. Their presence and love have been invaluable and I am deeply grateful for the role they have played in my life.

TABLE OF CONTENTS

LIST OF TABLES

TABLES

LIST OF FIGURES

FIGURES

LIST OF ABBREVIATIONS

ABBREVIATIONS

GWEC	Global Wind Energy Council
BEM	Blade Element Momentum
PARSEC	Parametric Section
NACA	National Advisory Committee for Aeronautics
NREL	National Renewable Energy Laboratory
RSM	Response Surface Methodology
CFD	Computational Fluid Dynamics
HAWC2	Horizontal Axis Wind turbine simulation Code 2nd generation

LIST OF SYMBOLS

SYMBOLS

Re	Reynolds number
t/c	Thickness-to-chord ratio
C_l	Lift coefficient
$C_{l\,max}$	Maximum lift coefficient
C_d	Drag coefficient
$C_{d\,min}$	Minimum drag coefficient
C_m	Moment coefficient
C_{l_α}	Lift curve slope
L/D	Lift-to-drag ratio
α	Angle of attack
α_{stall}	Angle of attack corresponding to stall
n_1	Power coefficient to extrapolate lift polar
n_2	Power coefficient to extrapolate drag polar
R^2	R-Squared value

CHAPTER 1

INTRODUCTION

In today’s developing world, the energy need of humanity is rising day by day, and the rate of depletion of non-renewable energy sources is increasing, as well. Therewith, human beings have inevitably increased the tendency to the usage of renewable energy alternatively in electricity generation. For example, many countries have developed various energy generation types to meet electricity demand from renewable energy sources like solar, wind, and hydro energy.

Out of the many types of renewable energy, wind energy stands out due to its numerous advantages. One of these advantages is its consistency in the long term, as it is available both during the day and at night. In addition, wind energy can be utilized in a variety of ways, from powering a single home with a single turbine to large-scale wind farms made up of multiple turbines.

Over the past two decades, the total installed capacity of wind turbines has seen a significant increase globally. Figure 1.1 illustrates the historical progression of total installations on a yearly basis since 2001. The Global Wind Report 2022, released by the Global Wind Energy Council (GWEC), reports that the total installed capacity for both onshore and offshore turbines has risen from 24 to 837 gigawatts worldwide in the last 20 years. This represents a significant growth in the use of wind energy as a source of renewable energy and highlights the increasing importance of wind energy in meeting the world's energy needs. Furthermore, this trend is expected to continue in the coming years, with many countries investing in the development and expansion of wind energy projects to meet their renewable energy targets.

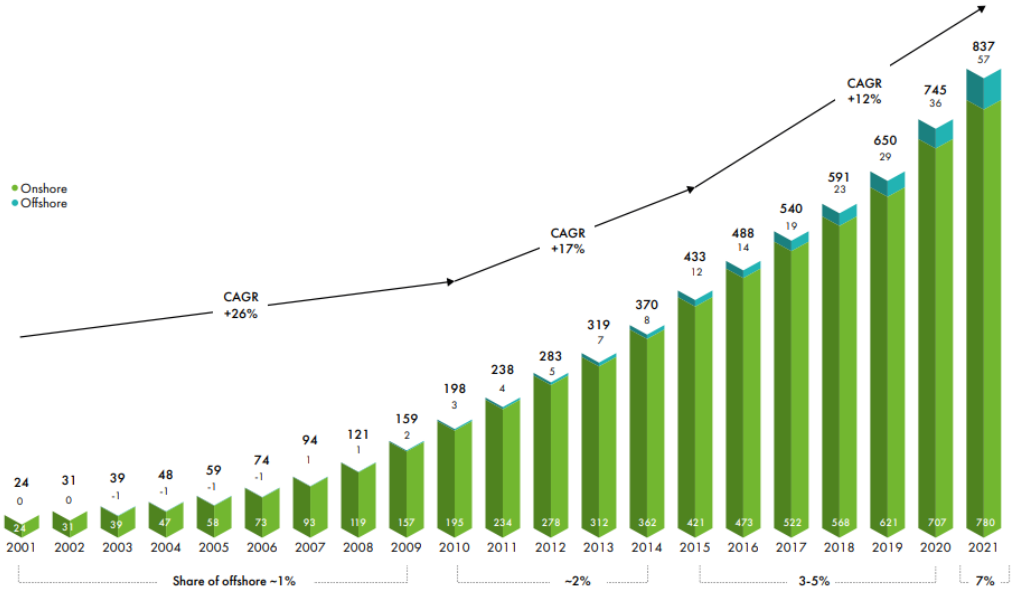

Figure 1.1. Historical development of total installations based on wind energy in the last twenty years. Image was taken from the Global Wind Report 2022 (2022).

The increase in the installed capacity of wind turbines in recent years can be attributed to not only the addition of new turbines but also the elevation of turbine hub heights. As the altitude increases, there are fewer obstacles, such as hills and buildings, which allows for more unrestricted airflow and more energy-rich wind, resulting in greater power-generating capability (Hartman, 2022). This approach not only increases the overall energy output of wind turbines but also allows for more efficient and cost-effective energy production.

Furthermore, the expansion of rotor diameters of turbines also contributes to the increase in installed capacity. This is due to the fact that larger blades can sweep a greater area in the air, allowing the wind turbine to capture more energy from the wind (Hartman, 2022). Additionally, the use of larger rotor diameters also enables turbines to capture wind energy from a wider range of wind speeds, which increases the turbine's capacity factor and, thus, the overall energy output.

As an example, Figure 1.2 illustrates the progression of hub height and rotor diameter for land-based wind turbines in the United States over time. As per data from the Land-Based Wind Market Report (Wiser et al., 2022), it can be observed that the hub height for wind turbines in the United States has increased significantly, rising from an average of 60 meters to around 100 meters. Similarly, the rotor diameter of these turbines has also grown, expanding from an initial 50 meters to a current average of 130 meters.

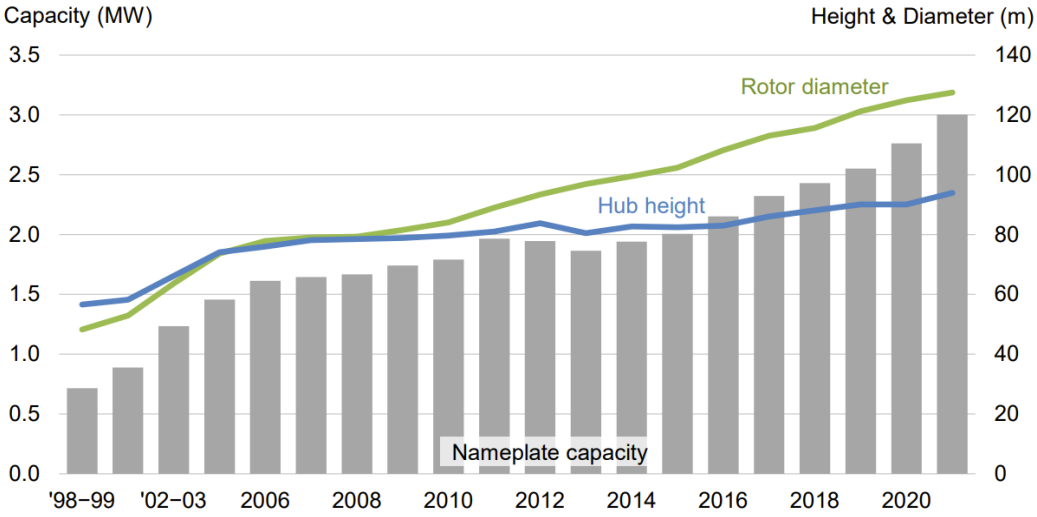

Figure 1.2. Historical growth in hub height and rotor diameter. Image was taken from Wiser et al. (2022).

Despite the benefits of larger blade diameters, there are some structural challenges that arise, such as increased gravitational and aerodynamic loading. One way to overcome these concerns is to increase the thickness of the airfoils, as thicker airfoils can improve structural efficiency and reduce the weight per unit of rotor diameter. This approach has been proposed by experts in the field, such as van Dam (2009), as a way to mitigate the structural issues associated with larger blade diameters and make wind turbines more reliable and durable. Additionally, thicker airfoils can also

help in increasing the resistance to fatigue and buckling, which are common issues in wind turbine blades.

A typical wind turbine blade uses a family of reasonably thick airfoils from 15 to 70+% thickness-to-chord ratio (t/c) distributed in an optimized fashion along its radius. Depending on the power level and the operational conditions of the wind turbine, as well as on their position along the radius, these airfoils will have to operate in certain Reynolds number ranges. As shown in Figure 1.3 (Ge et al., 2014), the local Reynolds number along the radius of the blade can vary significantly for wind turbines with different rated power levels, ranging from 200 kW to 12 MW. It can even reach as high as $14x10^6$ for a wind turbine rated at 12 MW.

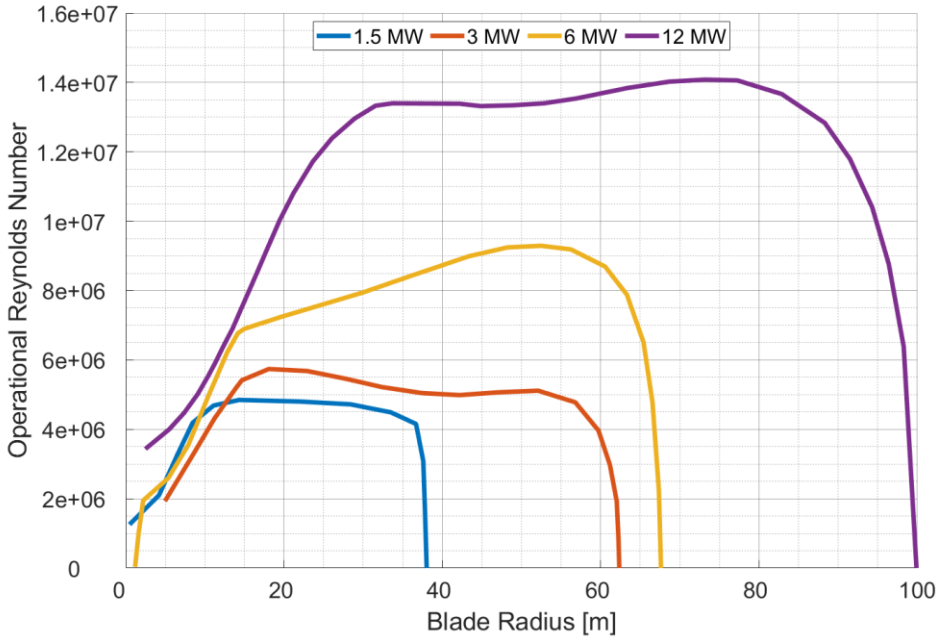

Figure 1.3. Typical operational Reynolds number variations along the blade radius for different size wind turbines. Data was taken from Ge et al. (2014).

Airfoil polars, which refer to the variations of aerodynamic lift and drag coefficients with angle of attack, are of critical importance in the design process of wind turbine blades. The main reason for this is that the optimization of a typical blade aerodynamic design heavily relies on the use of fast analysis tools based on the Blade Element Momentum (BEM) theory. These tools require accurate aerodynamic coefficient data for the airfoils that are intended to be used in the blade design as input, in order to effectively analyze and optimize the blade performance. Therefore, accurately determining the airfoil polars is essential for designing effective wind turbine blades.

During the development phase of a wind turbine airfoil, wind tunnel tests are generally conducted under limited Reynolds number conditions and often at lower Reynolds numbers than those encountered during operation. As a result, it is necessary to extrapolate the polar data to the relevant operational Reynolds numbers before it can be used in the design of the blade. However, the literature on this topic is limited and there are currently no well-established methods for extrapolating airfoil polar data from low to high Reynolds numbers. This is a significant challenge in the design process for the wind turbine industry.

1.1 Literature Review

Previous studies in the literature on the effects of Reynolds number on wind turbine airfoil aerodynamics can be broadly categorized into two groups. The first category comprises studies that primarily focus on the observation of the effects of Reynolds number through experimentation or analysis. The second category includes studies that aim to develop a methodology to predict the effects of Reynolds number on airfoil aerodynamics. There are many studies in the first category, but the number of studies in the second category is relatively limited. The following is a summary of some relevant research from the literature for both categories.

1.1.1 Reynolds Number Effects

Llorente et al. (2014) performed wind tunnel tests for three different airfoils, which are AWA18-1, DU 08-W-180, and DU 91-W2-250, up to $12x10^6$ Reynolds number. The results of the wind tunnel tests showed that the maximum lift coefficient ($C_{l\,max}$) increases with increasing Reynolds number. Moreover, their measurements showed that the angle of attack corresponding to stall (α_{stall}) is delayed as the Reynolds number increases. This is because, at higher Reynolds numbers, the flow around the airfoil becomes more turbulent, which leads to a more stable boundary layer. This stability leads to a delay in the onset of the stall, which allows the airfoil to operate at a relatively higher angle of attack.

Similarly, Sommers and Tangler (2000) drew the same conclusion for the maximum lift coefficient ($C_{l\,max}$) from the wind tunnel tests of S825 and S827 airfoils up to $6x10^6$ Reynolds number. Furthermore, the researchers also found that the minimum drag coefficient ($C_{d\,min}$) decreases with increasing Reynolds number for the same airfoils. This is because as the Reynolds number increases, the flow around the airfoil becomes more turbulent, which leads to a reduction in the thickness of the boundary layer and reduces drag.

Pires et al. (2016) conducted experiments on the DU00-W-212 airfoil up to $15x10^6$ Reynolds number and found similar results to previous studies in regards to the maximum lift coefficient ($C_{l\,max}$) and the minimum drag coefficient ($C_{d\,min}$). In addition to that, their measurements indicated that the lift curve slope (C_{L_α}) remains constant regardless of the increase in the Reynolds number.

In addition, Yamauchi and Johnson (1983) also conducted an investigation on experimental measurements of helicopter rotor airfoils. The results of their study showed that the variations in the maximum lift coefficient ($C_{l\,max}$) and the minimum drag coefficient ($C_{d\,min}$) with respect to the Reynolds number are consistent with the findings of other studies.

Another approach to understanding the high Reynolds number effects on wind turbine airfoils was reported by Ge et al. (2014) based on the RFOIL simulations. Their simulation results about the maximum lift coefficient ($C_{l\,max}$) and the minimum drag coefficient ($C_{d\,min}$) variations to the Reynolds number agree with experimental measurements. They also stated that the stall angle of attack is delayed with increasing Reynolds number. Additionally, a significant increase in the lift-to-drag (L/D) ratio was observed as the Reynolds number increased at the same angle of attack.

1.1.2 Reynolds Number Extrapolation Methods

As stated previously, available methodologies for Reynolds number extrapolation of aerodynamic coefficients are very scarce, and there is no well-established comprehensive methodology in the open literature. In this section, the existing methodologies in the literature are summarized.

Based on their literature search at the time, Yamauchi and Johnson (1983) investigated experimentally measured data of some thin NACA airfoils (mainly for helicopter rotors) and proposed a power law based methodology to predict the effect of Reynolds number variation on aerodynamic coefficients, especially for the maximum lift coefficient ($C_{l\,max}$) and minimum drag coefficient ($C_{d\,min}$) for the using below relations, respectively.

$$\frac{C_{l\,max}}{C_{l\,max\,Ref}} = \left(\frac{Re}{Re_{Ref}}\right)^{n_1} \qquad 1.1$$

$$\frac{C_{d\,min}}{C_{d\,min\,Ref}} = \left(\frac{Re}{Re_{Ref}}\right)^{n_2} \qquad 1.2$$

In these equations, the reference values are experimental data obtained at a reference Reynolds number, and the power coefficient values for $C_{l\,max}$ and $C_{d\,min}$ are suggested to have values between $0.125 < n_1 < 0.2$ and $-0.2 < n_2 < -0.125$ in their study, respectively.

Pettersson and Rizzi (2008) also proposed a similar methodology for scaling $C_{d\,min}$ to flight conditions for fixed-wing aeronautical applications, where the n_2 coefficient is suggested to have values from -0.2 (from Prandtl's turbulent flow analysis) to -0.11 (for airfoils operating at Reynolds numbers higher than 8 million). Regarding scaling of the lift curve with Reynolds number, Pettersson and Rizzi suggested a different methodology that starts with first scaling the lift curve slope based on a collection of experimental data for NACA 0012 (Mccroskey, 1987), extending this slope until the curve hits estimated $C_{l\,max}$ values from NACA airfoil data (Jacobs & Sherman, 1939) and applying similar post-stall characteristic as measured in the wind tunnel.

In another attempt to predict Reynolds number effects, especially for wind turbine applications, Wallman and Klein (2010) proposed applying calculated trends for Reynolds number effects using RFOIL (Timmer & van Rooij, 2003) simulation results and subsequently applying the predicted trends to reference experimental data to predict aerodynamic data at higher Reynolds numbers.

Ceyhan (2012) did a similar study as Wallmann and Klein using trends obtained from the RFOIL simulations in order to predict the high Reynolds number effects on a very large 20 MW wind turbine rotor design. Ceyhan proposed that adding the differences in polar data obtained from the RFOIL simulations to the measured data yields more reliable data at higher Reynolds numbers. Ceyhan's approach is outlined in the following equations.

$$C_l(\alpha, Re) = C_l(\alpha, Re_{test}) + \Delta C_{l,RFOIL} \qquad 1.3$$

$$\Delta C_{l,RFOIL} = C_{l,RFOIL}(\alpha, Re) - C_{l,RFOIL}(\alpha, Re_{test}) \quad 1.4$$

1.2 Objective and Scope of the Thesis

The objective of this thesis is to develop a data-driven approach for extrapolating Reynolds number using a power law method and to investigate its effectiveness in predicting aerodynamic coefficients and polars at higher Reynolds numbers.

In the context of this thesis, a data-driven approach to extrapolate the Reynolds number is proposed, and its prediction performance for airfoil aerodynamic polars is investigated. For this purpose, firstly, a database is constructed from experimentally obtained aerodynamic data from open literature for airfoils with thickness-to-chord ratio (t/c) values in the range of 15% to 30% in order to be more relevant to wind turbine blade design applications. Then, all available airfoil geometries are parameterized using PARSEC methodology, and a Pareto analysis is performed to understand the sensitivity of $C_{l\,max}$ and $C_{d\,min}$ variations to geometrical inputs as well as the Reynolds number using statistical tools. Based on this analysis, response surfaces are created to predict $C_{l\,max}$ and $C_{d\,min}$ of a given airfoil operating at a given Reynolds number. These predicted values are then utilized in a proposed power law based estimation methodology to obtain predictions for the full polars. This proposed method is tested for three different airfoil test cases for which the aerodynamic data are publicly available in a wide Reynolds number range.

1.3 Thesis Layout

This thesis is organized as follows:

In Chapter 2, the constructed experimental database and the proposed data-driven method based on power law are explained in detail.

In Chapter 3, the proposed method is tested for a group of airfoils, and the prediction performance of the method is represented.

In Chapter 4, predicted aerodynamic polars of FFA-W3-241 airfoil, a part of the reference wind turbine from the literature named DTU-10MW-RWT, are implemented to aeroelastic wind turbine simulations and predicted results are represented and compared with results existing in the literature.

Finally, in Chapter 5, the summary of the drawn conclusions and the suggestions for future works are given.

CHAPTER 2

METHODOLOGY

In this thesis, a data-driven methodology based on power law to extrapolate Reynolds number effects is proposed. The proposed method consists of 5 main parts.

Firstly, an experimental aerodynamic database of airfoils is constructed by using open literature. Secondly, all airfoils included in the database are inversely parameterized using the PARSEC method in order to enhance the database numerically in terms of the geometrical properties of the airfoils. Then, a principal sensitivity analysis, called Pareto analysis, is performed using a statistical tool to determine the most effective parameters among geometrical properties as well as the Reynolds number on $C_{l\,max}$ and $C_{d\,min}$ variations. After that step, in accordance with this analysis, two different response surfaces are generated to predict $C_{l\,max}$ and $C_{d\,min}$ of a given airfoil operating at a given Reynolds number. Lastly, these predicted values are used in a power law based estimation methodology to extend the predictions to full lift and drag polars. These five steps are explained thoroughly in the following sections and illustrated in Figure 2.1.

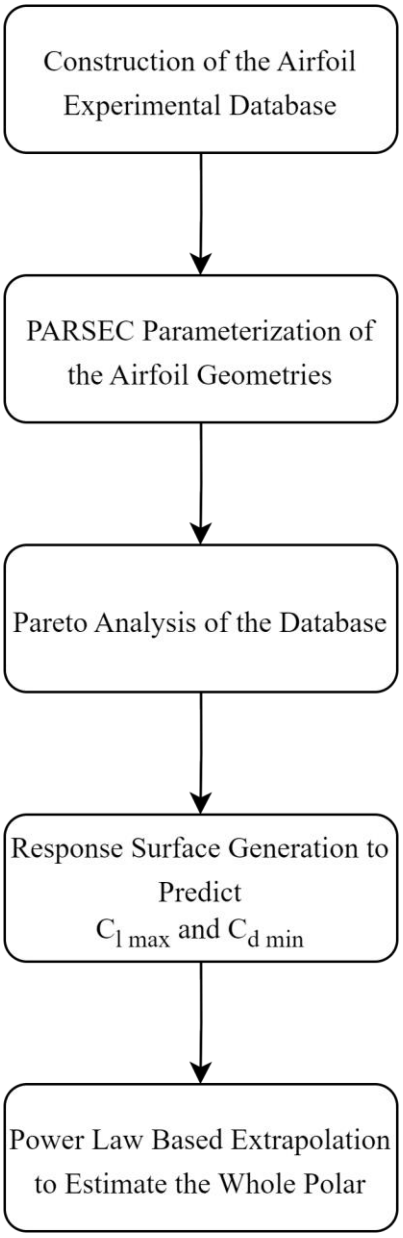

Figure 2.1. Summary diagram of the methodology part

2.1 Construction of the Airfoil Experimental Database

The experimental database is composed of 58 different airfoils with a thickness-to-chord ratio (t/c) within the range of 15-30% to be more related to wind turbine blade airfoils. Most of these airfoils are NACA profiles tested at Reynolds numbers $3x10^6$, $6x10^6$, and $9x10^6$, and digital form of data is available publicly (Abbott et al., 1945). Additionally, 4 different NREL S-Series airfoils, tested at Reynolds numbers generally from $1x10^6$ to $6x10^6$ are included in the database (Somers, 1997a, 1997b, 2005b, 2005a). Moreover, 6 wind turbine airfoils tested at Riso National Laboratory at Reynolds number generally around $1x10^6$ are also included in the database (Bertagnolio et al., 2001; Fuglsang et al., 1998). In addition, there are also a limited number of experimental datasets available in the literature for various other wind turbine airfoils as well. These are also included in the database.

All airfoils constructing the database are tabulated in Table 2.1. Additionally, the distribution of the thickness-to-chord ratio (t/c) for the constructed database is illustrated in Figure 2.2.

Table 2.1 Constructed experimental database for airfoil polars

Airfoil	***Reynolds Number [x10^{-6}]***	***Reference***
47 NACA Airfoils *	3, 6, 9	(Abbott et al., 1945)
S825	1, 2, 3, 4, 6	(Somers, 2005a)
S827	1, 2, 3, 4, 6	(Somers, 2005b)
S814	1, 2, 3	(Somers, 1997b)
S809	1, 1.5, 2	(Somers, 1997a)
DU91-W2-250 **	1, 1.5, 2, 3, 6, 9, 12	(Bertagnolio et al., 2001; Llorente et al., 2014; van Rooij & Timmer, 2003)

Table 2.1 Constructed experimental database for airfoil polars (Continued)

DU97-W-300 **	2, 2.5, 3	(van Rooij & Timmer, 2003)
DU93-W-210	1	(Bertagnolio et al., 2001)
FFA-W3-211	1.8	(Bertagnolio et al., 2001)
FX66-S196-V1	1.5	(Bertagnolio et al., 2001)
FFA-W3-241	1.6	(Fuglsang et al., 1998)
FFA-W3-301	1.6	(Fuglsang et al., 1998)

*47 NACA Airfoils are listed in detail in Appendix A.

**Only C_l polar data is available.

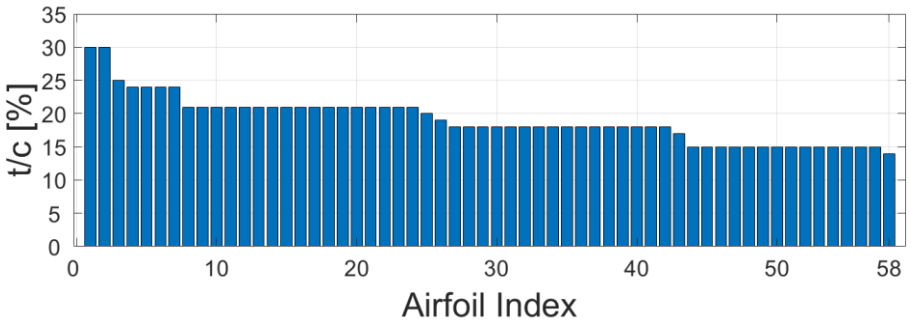

Figure 2.2. Thickness-to-chord ratio (t/c) distribution of the constructed airfoil database

2.2 PARSEC Parameterization of Airfoil Geometries

The PARSEC method, an acronym for "Parametric Section", is an airfoil parameterization scheme developed by Sobieczky (1997). This method expresses the airfoil geometry using the linear combination of the functions based on 12 specific airfoil geometrical properties. These geometrical properties, called PARSEC parameters, are illustrated in Figure 2.3 and listed in Table 2.2.

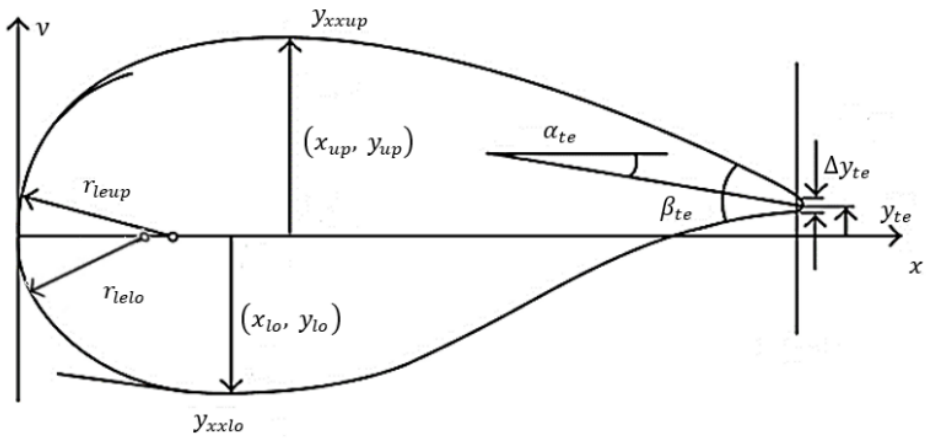

Figure 2.3. PARSEC parameters for an airfoil geometry. Image was taken from Akram & Kim (2021).

Table 2.2 Definitions of PARSEC parameters

Parameter	***Definition***	***Symbology***
p_1	The Leading-Edge Radius for Upper Curve	$r_{LE\ upper}$
p_2	The Leading-Edge Radius for Lower Curve	$r_{LE\ lower}$
p_3	The Maximum Thickness x Location for Upper Curve	x_{upper}
p_4	The Maximum Thickness y Location for Upper Curve	y_{upper}
p_5	The Upper Crest Curvature	$y_{xx\ upper}$
p_6	The Maximum Thickness x Location for Lower Curve	x_{lower}
p_7	The Maximum Thickness y Location for Lower Curve	y_{lower}
p_8	The Lower Crest Curvature	$y_{xx\ lower}$
p_9	The Trailing Edge Thickness	Δy_{TE}
p_{10}	The Trailing Edge Position	y_{TE}
p_{11}	The Trailing Edge Angle	α_{TE}
p_{12}	The Trailing Wedge Angle	β_{TE}

The general formulation of the PARSEC method is defined separately for upper and lower surfaces by using the 6^{th} order polynomials as follows.

$$y_{upper} = \sum_{n=1}^{6} A_{upper\ n}\, x^{n-\frac{1}{2}} \tag{2.1}$$

$$y_{lower} = \sum_{n=1}^{6} A_{lower\ n}\, x^{n-\frac{1}{2}} \tag{2.2}$$

In these equations, y_{upper} and y_{lower} represent the y coordinates of the upper and lower surfaces of the airfoil geometry, respectively, of an airfoil geometry. The variable x represents the chordwise coordinate, and A_{upper} and A_{lower} are the weight coefficients. These weight coefficients are determined by solving the following two linear systems of equations using 12 PARSEC parameters for upper and lower surfaces, respectively, as shown below.

$$C_{upper}\, A_{upper} = B_{upper} \tag{2.3}$$

$$C_{lower}\, A_{lower} = B_{lower} \tag{2.4}$$

where

$$C_{upper} = \begin{bmatrix} 1 & 1 & 1 & 1 & 1 & 1 \\ p_3^{\frac{1}{2}} & p_3^{\frac{3}{2}} & p_3^{\frac{5}{2}} & p_3^{\frac{7}{2}} & p_3^{\frac{9}{2}} & p_3^{\frac{11}{2}} \\ \frac{1}{2} & \frac{3}{2} & \frac{5}{2} & \frac{7}{2} & \frac{9}{2} & \frac{11}{2} \\ \frac{1}{2}p_3^{-\frac{1}{2}} & \frac{3}{2}p_3^{\frac{1}{2}} & \frac{5}{2}p_3^{\frac{3}{2}} & \frac{7}{2}p_3^{\frac{5}{2}} & \frac{9}{2}p_3^{\frac{7}{2}} & \frac{11}{2}p_3^{\frac{9}{2}} \\ -\frac{1}{4}p_3^{-\frac{3}{2}} & \frac{3}{4}p_3^{-\frac{1}{2}} & \frac{15}{4}p_3^{\frac{1}{2}} & \frac{35}{4}p_3^{\frac{3}{2}} & \frac{63}{4}p_3^{\frac{5}{2}} & \frac{99}{4}p_3^{\frac{7}{2}} \\ 1 & 0 & 0 & 0 & 0 & 0 \end{bmatrix} \quad 2.5$$

$$B_{upper} = \begin{bmatrix} p_{10} + p_9/2 \\ p_4 \\ \tan\left(-p_{11} - \frac{p_{12}}{2}\right) \\ 0 \\ p_5 \\ \sqrt{2p_1} \end{bmatrix} \quad 2.6$$

$$C_{lower} = \begin{bmatrix} 1 & 1 & 1 & 1 & 1 & 1 \\ p_6^{\frac{1}{2}} & p_6^{\frac{3}{2}} & p_6^{\frac{5}{2}} & p_6^{\frac{7}{2}} & p_6^{\frac{9}{2}} & p_6^{\frac{11}{2}} \\ \frac{1}{2} & \frac{3}{2} & \frac{5}{2} & \frac{7}{2} & \frac{9}{2} & \frac{11}{2} \\ \frac{1}{2}p_6^{-\frac{1}{2}} & \frac{3}{2}p_6^{\frac{1}{2}} & \frac{5}{2}p_6^{\frac{3}{2}} & \frac{7}{2}p_6^{\frac{5}{2}} & \frac{9}{2}p_6^{\frac{7}{2}} & \frac{11}{2}p_6^{\frac{9}{2}} \\ -\frac{1}{4}p_6^{-\frac{3}{2}} & \frac{3}{4}p_6^{-\frac{1}{2}} & \frac{15}{4}p_6^{\frac{1}{2}} & \frac{35}{4}p_6^{\frac{3}{2}} & \frac{63}{4}p_6^{\frac{5}{2}} & \frac{99}{4}p_6^{\frac{7}{2}} \\ 1 & 0 & 0 & 0 & 0 & 0 \end{bmatrix} \quad 2.7$$

$$B_{lower} = \begin{bmatrix} p_{10} - p_9/2 \\ p_7 \\ \tan\left(-p_{11} + \frac{p_{12}}{2}\right) \\ 0 \\ p_8 \\ -\sqrt{2p_2} \end{bmatrix} \quad 2.8$$

Lastly, the solved form of linear systems of equations to determine the weight coefficients can be written for upper and lower surfaces, respectively.

$$A_{upper} = C_{upper}^{-1} B_{upper} \quad 2.9$$

$$A_{lower} = C_{lower}^{-1} B_{lower} \quad 2.10$$

2.2.1 PARSEC Parameterization Validation

All airfoils, including in the constructed database, are parameterized using the PARSEC methodology through the CB2: Airfoil Optimization with GUI tool (Bellini et al., 2017). As a PARSEC parameterization validation study, the NREL S827 airfoil was chosen as the reference airfoil. The PARSEC parameters were calculated by inputting the original airfoil coordinates into the CB2 tool and are listed in Table 2.3. The airfoil geometry was then generated using the calculated parameters and compared to the original geometry. As shown in Figure 2.4, the generated geometry using the PARSEC methodology is nearly identical to the original geometry.

Table 2.3 Calculated PARSEC parameters for NREL S827 airfoil

Parameter	***Value***
p_1	0.0134
p_2	0.0070
p_3	0.4847
p_4	0.1167
p_5	-0.8680
p_6	0.4337
p_7	-0.0929
p_8	1.5193
p_9	0
p_{10}	0
p_{11}	5.4864
p_{12}	12.7025

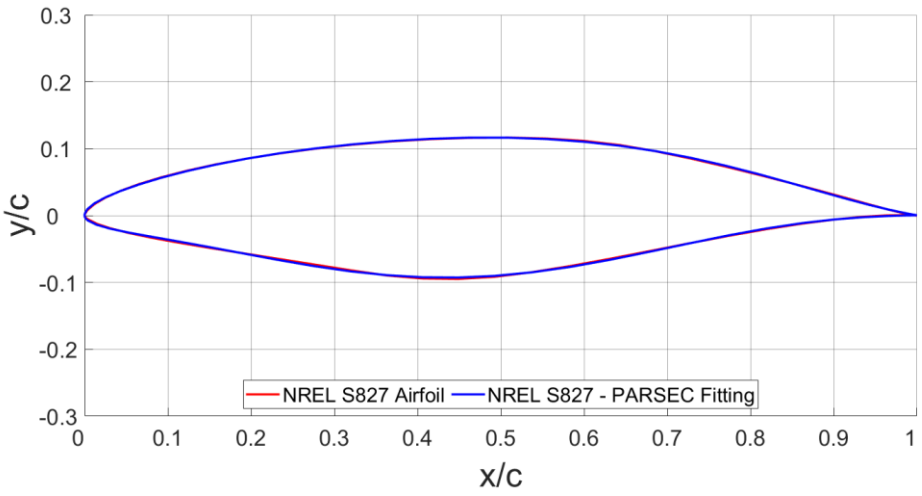

Figure 2.4. Original and PARSEC parameterized comparison of NREL S827 airfoil

2.3 Pareto Analysis of the Database

The constructed airfoil database is analyzed to determine which parameters (i.e., 12 PARSEC parameters plus the Reynolds number, so 13 parameters in total) play a dominant role in the variations of $C_{l\,max}$ and $C_{d\,min}$. The Pareto analysis study is performed by fitting the airfoil database to the first-order model in order to see the effect of each parameter individually via the statistical analysis software JMP (2015). In this analysis, the effects of the parameters used in the model are quantified with a t-ratio, and it represents the significance level of the effect of each parameter in the response (Kappanman, 1971; Pfanzagl & Sheynin, 1996).

Figure 2.5 illustrates the distribution of the most influential parameters in the variations of $C_{l\,max}$ and $C_{d\,min}$ data obtained as a result of the Pareto analysis. Considering the results for the $C_{l\,max}$ data (Figure 2.5a), the Reynolds number was found to be the most dominant parameter. This is expected because the stability of the boundary layer highly depends on the Reynolds number, and this stability directly affects the onsetting of the stall. The Reynolds number was followed by the maximum thickness of the lower surface (p_7), which reduces the lift coefficient due to the separation of the flow from the surface. The parameters p_9 and p_{10}, which correspond to the trailing edge thickness and position, appear to have no impact on the variations in $C_{l\,max}$ variations because these parameters were equal to zero for all airfoils included in the constructed database. With regard to the results for the $C_{d\,min}$ data (Figure 2.5b), it was observed that, in contrast to the $C_{l\,max}$ case, the leading-edge radius of the upper surface (p_1) was found to be the most dominant parameter. This parameter was followed by the Reynolds number. This is also expected because with increasing Reynolds number, the flow becomes more turbulent, which leads to a reduction in the thickness of the boundary layer and reduces drag. Similar to the results of the $C_{l\,max}$ data analysis, the parameters p_9 and p_{10} are the least influential parameters for $C_{d\,min}$ as well. In addition, p_{11} and p_{12}, which correspond to the trailing edge angle and the trailing wedge angle, have a minimal effect on $C_{d\,min}$.

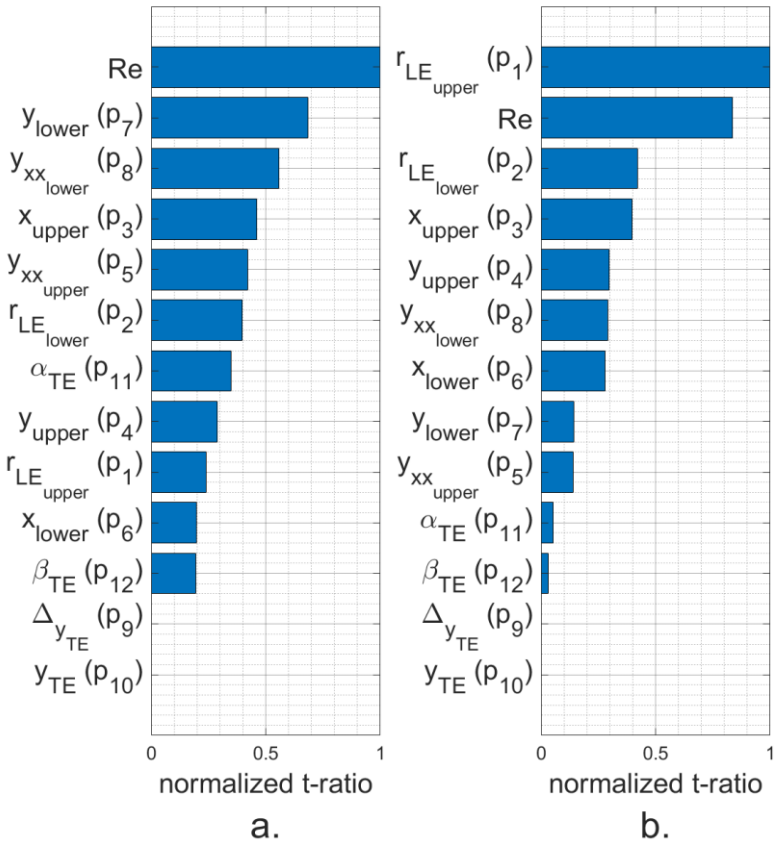

Figure 2.5. Pareto Analysis results showing the significance level of the parameters in the variations of (a) $C_{l\,max}$ and (b) $C_{d\,min}$, based on the constructed airfoil database

2.4 Response Surface Generation to Predict $C_{l\,max}$ & $C_{d\,min}$ at a given Reynolds Number

Response Surface Methodology (RSM) is a statistical technique that can be used to establish a mathematical connection between input and output variables (Khuri & Mukhopadhyay, 2010). If the mathematical relationship between input and output variables is uncertain, RSM can be used to approximate it by utilizing a low-degree polynomial model as written below.

$$y = f'(x)\beta + \varepsilon \qquad 2.11$$

The function $f'(x)$ is composed of elements that involve powers and cross-products of $x_1, x_2, \ldots, x_k$ up to a certain degree. The coefficients in the function, referred to as parameters, are represented by β and ε represents a random experimental error with a zero mean. A common model used in Response Surface Methodology is the second-degree model, which can be expressed as:

$$y = \beta_0 + \sum_{i=1}^{k} \beta_i x_i + \sum_{i<j} \sum \beta_{ij} x_i x_j + \sum_{i=1}^{k} \beta_{ii} {x_i}^2 + \varepsilon \qquad 2.12$$

The constructed airfoil database is used to generate two separate second-degree model response surface equations (in the form of Equation 2.12), one for $C_{l\,max}$ and one for $C_{d\,min}$ prediction, using the statistical analysis tool JMP (2015), according to the schematic given below:

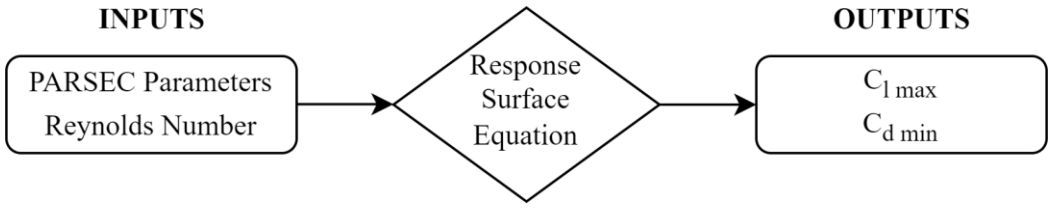

Figure 2.6. Schematic used for generating a response surface using the constructed airfoil database

The response surface equations were generated using the first 7 parameters outlined in Figure 2.5, based on the outcomes of the Pareto analysis. Figures 2.7a and 2.7b

demonstrate the accuracy of the response surface predictions through a comparison of actual and predicted values for $C_{l\,max}$ and $C_{d\,min}$, respectively. The majority of the data aligns with the expected values shown by the 45-degree line in both predictions. The R^2 value, which is a numerical value between 0 and 1 representing strength of the fitted model proportionally to the exact dataset, is 0.948 and 0.95 for $C_{l\,max}$ and $C_{d\,min}$, respectively, indicating a high level of accuracy. Figures 2.8a and 2.8b show the variations of the R^2 parameter with the number of inputs used for the generation of response surfaces for $C_{l\,max}$ and $C_{d\,min}$, respectively. As one can see, the variation converges as the number of input parameters is increased, and the variation is not significant after about 7 input parameters are used. The generated response surface equations for $C_{l\,max}$ and $C_{d\,min}$ can be found in Appendix B and C, respectively.

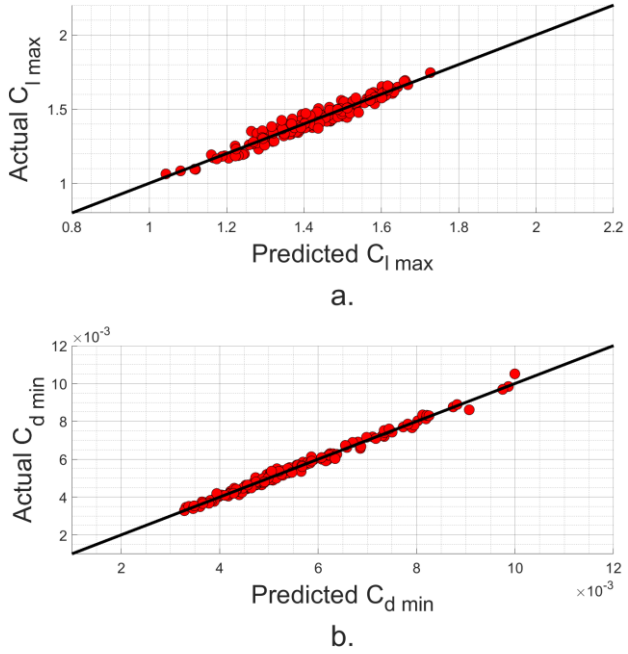

Figure 2.7. Actual vs. Predicted comparisons for (a) $C_{l\ max}$ (b) $C_{d\ min}$

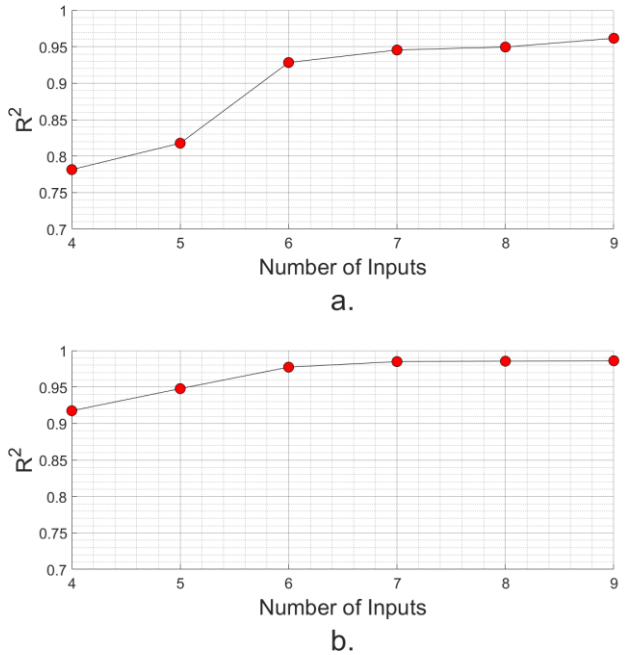

Figure 2.8. Convergence of R^2 with the number of inputs used for response surface generation for (a) $C_{l\ max}$ and (b) $C_{d\ min}$

2.5 Power Law Based Extrapolation to Estimate the Whole Polar

Yamauchi and Johnson (1983) proposed a power law based method to predict the effect of Reynolds number variation on $C_{l\,max}$ and $C_{d\,min}$ using,

$$\frac{C_{l\,max}}{C_{l\,max\,Ref}} = \left(\frac{Re}{Re_{Ref}}\right)^{n_1} \quad 2.13$$

$$\frac{C_{d\,min}}{C_{d\,min\,Ref}} = \left(\frac{Re}{Re_{Ref}}\right)^{n_2} \quad 2.14$$

Here, the reference values are experimental data obtained at a reference Reynolds number, and the power coefficient values for $C_{l\,max}$ and $C_{d\,min}$ are suggested to have values between $0.125<n_1<0.2$ and $-0.2<n_2<-0.125$ in their study, respectively.

Here, this power law extrapolation methodology proposed for only two coefficients is extended to full polars of airfoils. The polar extrapolation for C_l-α variations is performed following the below procedure, assuming data at a reference condition is available:

1) Calculate PARSEC parameters for a given airfoil shape.
2) Estimate the $C_{l\,max}$ value for a required Reynolds number using the response surface equation.
3) Using the $C_{l\,max\,Ref}$ value at a reference Reynolds number and the estimated $C_{l\,max}$ value at the required Reynolds number, calculate n_1 from Equation 2.13.
4) For each angle of attack between negative stall and positive stall for the reference data, hence mostly in the linear range, scale this n_1 value using local relative lift curve slope using,

$$\tilde{n}_1 = n_1 \left[\frac{\left| C_{l_{\alpha_i}} - C_{l_{\alpha @ \alpha=0}} \right|}{\max\left(\left| C_{l_{\alpha_i}} - C_{l_{\alpha @ \alpha=0}} \right| \right)} \right] \quad 2.15$$

where $C_{l_{\alpha_i}}$ is the local lift curve slope at the selected angle of attack and $C_{l_{\alpha @ \alpha=0}}$ is the lift curve slope at 0° angle of attack. This step makes sure that during extrapolation, the values in the linear region will basically remain constant if the lift curve slope is constant. In previous studies, it was shown that the Reynolds dependence within the linear region is weak (Pires et al., 2016).

5) In the post-stall regions (negative or positive), use the original n_1.
6) At each angle of attack, use the same n values to extrapolate the angle of attack values as well for the required Reynolds number.

Regarding the scaling of drag polars, when the constructed database is investigated, it is observed that while the drag bucket expands with increasing Reynolds number, the drag coefficients outside of the drag bucket change minimally with Reynolds number. The reason for this minimal change in drag values outside of the drag bucket is that as the angle of attack increases, the pressure drag component becomes more dominant in the overall drag, making the drag values less dependent on the shape of the airfoil. Therefore, while extrapolating the measured C_d coefficients to a higher Reynolds number, to use the n_2 value coming from $C_{d\,min}$ estimations is suggested only inside the drag bucket. So, the C_d extrapolation procedure is,

1) Calculate PARSEC parameters for a given airfoil shape.
2) Estimate the $C_{d\,min}$ value for a required Reynolds number using the response surface equation.

3) Using the $C_{d\,min\,Ref}$ value at a reference Reynolds number and the estimated $C_{d\,min}$ value at the required Reynolds number, calculate n_2 from Equation 2.14.
4) Use this n_2 value for extrapolating for all C_d values within the drag bucket.
5) Use the $-n_2$ value to extrapolate the angle of attack values as well (Because the drag bucket expands with increasing Reynolds number.).
6) Keep C_d values constant outside the drag bucket, if available.

CHAPTER 3

AIRFOIL AERODYNAMIC POLAR PREDICTIONS

The Reynolds number extrapolation methodology explained in Chapter 2 is tested for three different airfoil cases in two groups. The first group consists of an airfoil included in constructed airfoil database, which is NACA $65_{(3)}618$. The second group consists of DU00-W-212 and NACA $63_{(3)}018$ airfoils not included in the database. The main aim of the testing dividing into two groups is to make a comparison between the prediction performance of the airfoils that are included in the dataset and the not included ones.

Since the constructed airfoil database consists of mostly NACA airfoil profiles, it is important to see prediction performance for a NACA profile. Due to this reason, NACA $65_{(3)}618$ airfoil with 18% thickness is selected as the test case for the first group. Polar data of this airfoil is available at Reynolds numbers $3x10^6$, $6x10^6$ and $9x10^6$ (Abbott et al., 1945).

The first case of the second group is the 21% thick DU00-W-212 airfoil, which was tested extensively in DNW-HDG wind tunnel in the context of the AVATAR project (Pires et al., 2016) and polar data are available at Reynolds numbers $3x10^6$, $6x10^6$, $9x10^6$, $12x10^6$ and $15x10^6$. The second test case of the second group is the 18% thick symmetrical NACA $63_{(3)}018$ airfoil for which the aerodynamic polar data are available at $3x10^6$, $6x10^6$, $9x10^6$, $15x10^6$ and $20x10^6$ (Loftin & Bursnall, 1948).

These 3 airfoil test cases and their available data are summarized with respect to the their group in Table 3.1.

Table 3.1 Tested airfoil cases and available measurements

Airfoil	***Reynolds Number [x10^{-6}]***	***Group Number****
NACA 65$_{(3)}$618	3, 6, 9	1
DU00-W-212	3, 6, 9, 12, 15	2
NACA 63$_{(3)}$018	3, 6, 9, 15, 20	2

*Group 1: Included in the database, Group 2: Not included in the database

In the following parts, firstly, tables present a comparison of experimentally measured $C_{l\,max}$ and $C_{d\,min}$ values, respectively, with the predicted ones using the generated response surfaces for all test cases at available Reynolds numbers. For the first group, airfoil that were included in the database, the results of NACA 65$_{(3)}$618 are presented in Table 3.2-3.3. For the second group, airfoils that were not included in the database, the results for DU00-W-212 and NACA 63$_{(3)}$018 are presented in Table 3.5-3.6 and Table 3.8-3.9, respectively. The prediction errors for $C_{l\,max}$ and $C_{d\,min}$ values defined as,

$$\text{Error for } C_{l\,max}[\%] = \frac{\text{Pred } C_{l\,max} - \text{Exp } C_{l\,max}}{\text{Exp } C_{l\,max}} \text{ x } 100 \qquad 3.1$$

$$\text{Error for } C_{d\,min}[\%] = \frac{\text{Pred } C_{d\,min} - \text{Exp } C_{d\,min}}{\text{Exp } C_{d\,min}} \text{ x } 100 \qquad 3.2$$

are also presented in these tables.

Then, using the measured $C_{l\,max}$ and $C_{d\,min}$ at a reference Reynolds number and the predicted ones, power law coefficients are calculated and implemented in the methodology explained in Section 2.5 to predict the full lift and drag polars. The calculated n_1 and n_2 coefficients (obtained from Equations 2.13 and 2.14) are

presented in Tables 3.4, 3.7 and 3.10 for NACA $65_{(3)}618$, DU00-W-212 and NACA$63_{(3)}018$ airfoils, respectively.

3.1 Predictions for an Airfoil Included in Database

In this section, prediction performance for the NACA $65_{(3)}618$ airfoil is represented in detail. Tables 3.2 and 3.3 present a comparison of experimentally measured $C_{l\,max}$ and $C_{d\,min}$ values, respectively, with the predicted ones using the generated response surfaces.

Table 3.2 $C_{l\,max}$ predictions for NACA $65_{(3)}618$ airfoil

Re [x10^{-6}]	$C_{l\,max}$ ***(Experimental)***	$C_{l\,max}$ ***(Predicted)***	***Error [%]***
3	1.40711	1.40808	0.07
6	1.54678	1.53591	-0.70
9	1.65188	1.61916	-1.98

Table 3.3 $C_{d\,min}$ predictions for NACA $65_{(3)}618$ airfoil

Re [x10^{-6}]	$C_{d\,min}$ ***(Experimental)***	$C_{d\,min}$ ***(Predicted)***	***Error [%]***
3	0.00551	0.00538	-2.31
6	0.00476	0.00469	-1.53
9	0.00429	0.00441	2.91

Regarding both $C_{l\,max}$ and $C_{d\,min}$ predictions for the NACA $65_{(3)}618$ airfoil, error percentage levels for all Reynolds number cases are really low, at less than 3%. This is expected and obvious because this airfoil is already included in the constructed database. Also, existing of many similar airfoils in the database can be another reason since the database consists of mostly NACA airfoils measured at the same Reynolds number values.

Using the measured $C_{l\,max}$ and $C_{d\,min}$ values at Re=$3x10^6$ as a reference and the predicted ones at higher Reynolds numbers, the power coefficients are calculated using Equations 2.13 and 2.14. The calculated n_1 and n_2 coefficients are tabulated in Table 3.4 for each extrapolation case.

Table 3.4 n_1 and n_2 coefficients for extrapolation cases of NACA $65_{(3)}618$ airfoil

Extrapolation Case (Reference Re → Target Re)	n_1	n_2
3 → 6	0.1264	-0.2333
3 → 9	0.1278	-0.2017

While the calculated n_1 values are within the ranges proposed by Yamauchi & Johnson (1983) (i.e., $0.125<n_1<0.2$ for $C_{l\,max}$ and $-0.2<n_2<-0.125$ for $C_{d\,min}$), the calculated n_2 values are out of the ranges. However, being out of the proposed ranges for calculated power values can be normal because their investigation was focused on the helicopter rotor airfoils, having relatively lower thicknesses.

Figures 3.1 and 3.2 present comparisons of predicted C_l-α variations with the experimental data with the predictions obtained using the method proposed by Ceyhan (2012), which is based on using Reynolds number dependency trends obtained from RFOIL simulations. In general, both methods seem to predict

reasonably close results to each other. However, the prediction results are closer to the experimental data with the current method mainly because of its better $C_{l\,max}$ prediction capability. Furthermore, the stall angle of attack (α_{stall}) shift to higher angles is much better predicted with the current method compared to the method proposed in Ceyhan (2012). Regarding the post-stall characteristics, while Ceyhan's method is underpredicting the lift coefficient values, the current method predicts more successfully.

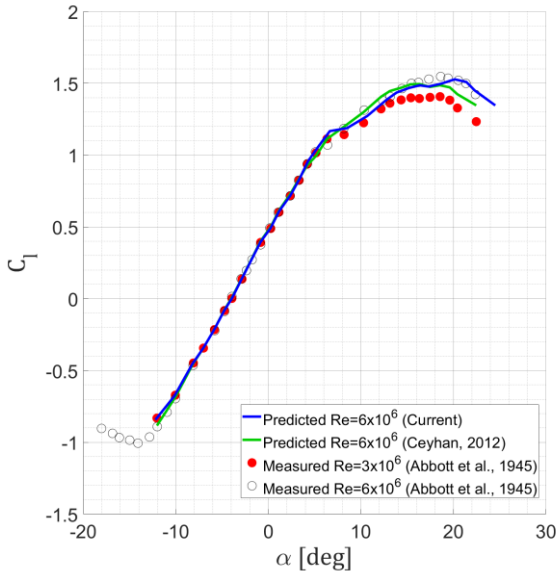

Figure 3.1. Comparison of predicted C_l-α variations with the measured data and the predictions obtained by the method of Ceyhan (2012) for NACA $65_{(3)}618$ airfoil at Re=6x10^6. Measured data at Re=3x10^6 is used as the reference point.

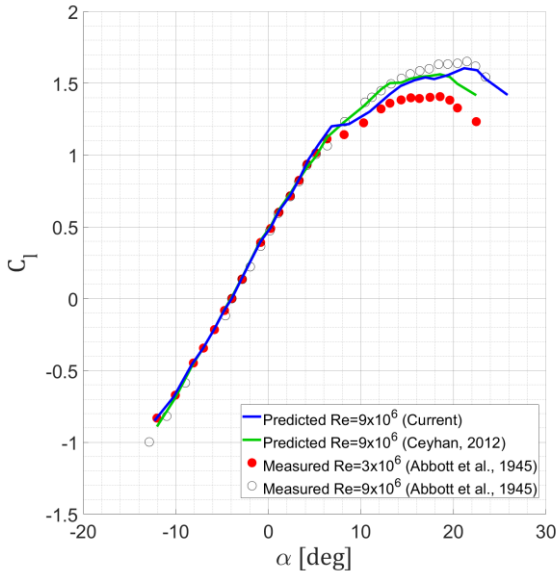

Figure 3.2. Comparison of predicted C_l-α variations with the measured data and the predictions obtained by the method of Ceyhan (2012) for NACA $65_{(3)}618$ airfoil at Re=9x10^6. Measured data at Re=3x10^6 is used as the reference point.

Figures 3.3 and 3.4 present comparisons of predicted C_d-α variations with the experimental data with the predictions obtained using the method proposed by Ceyhan (2012). Generally, $C_{d\,min}$ levels are reasonably well predicted by both methods. Regarding the predictions for the expansion in the drag bucket, Ceyhan's method predicts the change in size better than the current method for this airfoil case at both Reynolds number values.

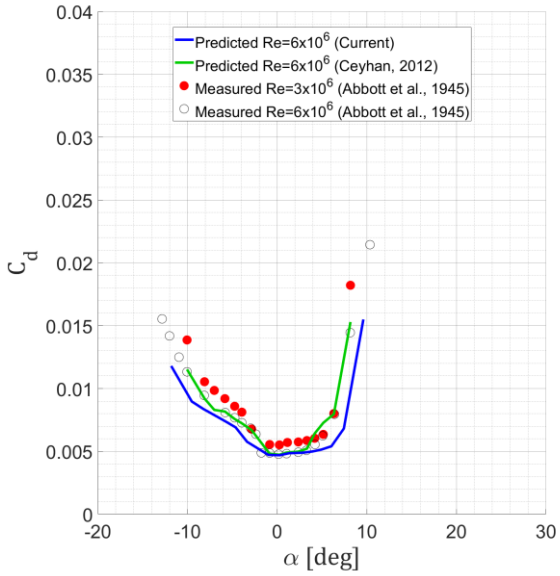

Figure 3.3. Comparison of predicted C_d-α variations with the measured data and the predictions obtained by the method of Ceyhan (2012) for NACA $65_{(3)}618$ airfoil at Re=6x10^6. Measured data at Re=3x10^6 is used as the reference point.

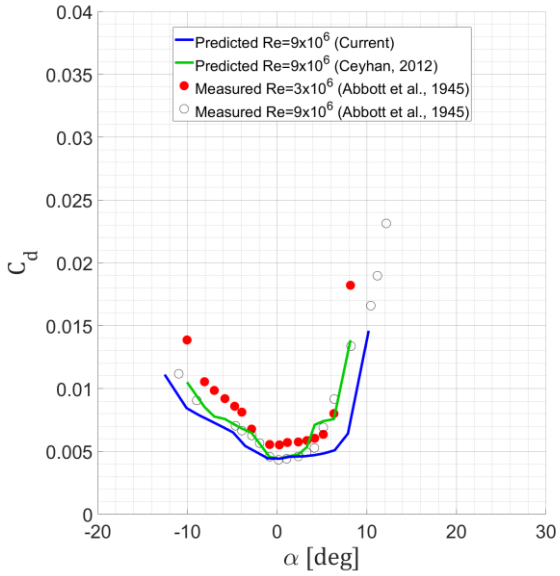

Figure 3.4. Comparison of predicted C_d-α variations with the measured data and the predictions obtained by the method of Ceyhan (2012) for NACA $65_{(3)}618$ airfoil at Re=9x10^6. Measured data at Re=3x10^6 is used as the reference point.

3.2 Predictions for Airfoils not Included in Database

3.2.1 Predictions for DU00-W-212 Airfoil

In this section, the prediction performance for the DU00-W-212 airfoil, which is not included in the constructed database, is represented in detail. Tables 3.5 and 3.6 present a comparison of experimentally measured $C_{l\,max}$ and $C_{d\,min}$ values, respectively, with the predicted ones using the generated response surfaces.

Table 3.5 $C_{l\,max}$ predictions for DU00-W-212 airfoil

Re [x10^{-6}]	$C_{l\,max}$ ***(Experimental)***	$C_{l\,max}$ ***(Predicted)***	***Error [%]***
3	1.29450	1.28490	-0.74
6	1.45890	1.46020	0.09
9	1.55590	1.59092	2.25
12	1.62500	1.67707	3.20
15	1.65660	1.71864	3.75

Table 3.6 $C_{d\,min}$ predictions for DU00-W-212 airfoil

Re [x10^{-6}]	$C_{d\,min}$ ***(Experimental)***	$C_{d\,min}$ ***(Predicted)***	***Error [%]***
3	0.00700	0.00691	-1.30
6	0.00601	0.00591	-1.67
9	0.00566	0.00533	-5.78
12	0.00558	0.00518	-7.17
15	0.00548	0.00545	-0.55

Regarding the $C_{l\,max}$ predictions presented in Table 3.5 for the DU00-W-212 airfoil, the error percentage levels are generally overpredicted except for Re=3x10^6 case. Nevertheless, the error levels are reasonably low, with the maximum error being about 3.75%. For $C_{d\,min}$ predictions presented in Table 3.6, unlike the $C_{l\,max}$ predictions, an underprediction for all cases is seen, and the maximum error level is about -7.17%. Considering that this airfoil is not included in the database, it can be deduced that the prediction performance for $C_{l\,max}$ and $C_{d\,min}$ is really well.

Table 3.7 shows the calculated n_1 and n_2 coefficients for each extrapolation case. Similar to NACA $65_{(3)}$618 case, the calculated n_2 values are not mostly within the ranges proposed by Yamauchi and Johnson (1983); however, the n_1 values fall within the ranges.

Table 3.7 n_1 and n_2 coefficients for extrapolation cases of DU00-W-212 airfoil

Extrapolation Case (Reference Re → Target Re)	n_1	n_2
3 → 6	0.1738	-0.2443
3 → 9	0.1877	-0.2476
3 → 12	0.1868	-0.2172
3 → 15	0.1761	-0.1555

Figures 3.5 and 3.6 present comparisons of predicted C_l-α variations with the experimental data with the predictions obtained using the method proposed by Ceyhan (2012) for Reynolds numbers 6x10^6 and 9x10^6, respectively. While Ceyhan's method significantly underestimates the change in $C_{l\,max}$ value with increasing Reynolds number, the current method is able to predict more accurately. This is mainly due to the current method's stronger ability to predict $C_{l\,max}$. Moreover, it can be seen that the current method captures the angle of attack

corresponding to stall more successfully. Considering the post-stall predictions, it is deduced that the current method overpredicts in the positive post-stall region, whereas negative post-stall characteristics are reasonably well predicted.

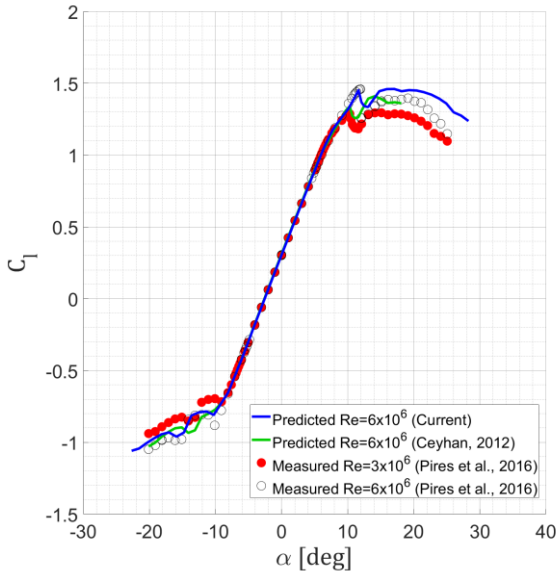

Figure 3.5. Comparison of predicted C_l-α variations with the measured data and the predictions obtained by the method of Ceyhan (2012) for DU00-W-212 airfoil at Re=6x10^6. Measured data at Re=3x10^6 is used as the reference point.

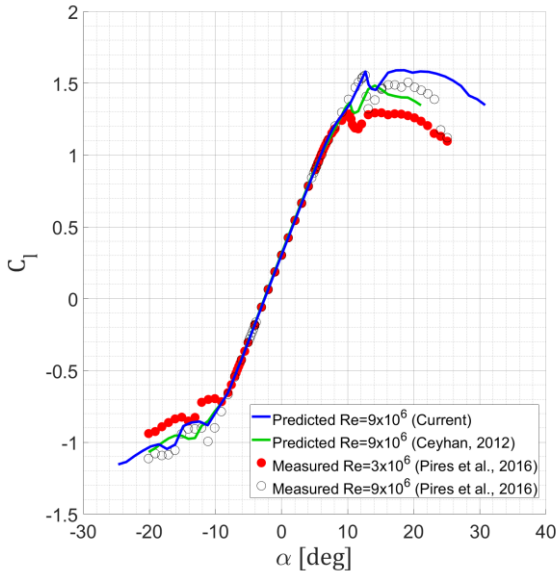

Figure 3.6. Comparison of predicted C_l-α variations with the measured data and the predictions obtained by the method of Ceyhan (2012) for DU00-W-212 airfoil at Re=9x10^6. Measured data at Re=3x10^6 is used as the reference point.

Figures 3.7 and 3.8 show comparisons of predicted C_l-α variations with the experimental data with the predictions obtained using the method proposed by Ceyhan (2012) for Reynolds numbers 12x10^6 and 15x10^6, respectively. Although there is only 1 airfoil out of 58 existed in the database at a Reynolds number that is higher than Re=9x10^6, i.e. Re=12x10^6 for DU91-W2-250 airfoil, the predictions for C_l-α variations of the DU00-W-212 airfoil have good agreement with the experimentally measured data at Re=12x10^6 and Re=15x10^6, with differences observed again in the positive post-stall region.

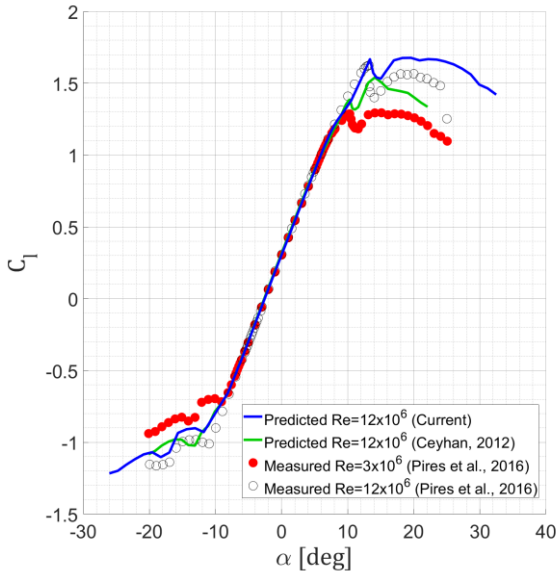

Figure 3.7. Comparison of predicted C_l-α variations with the measured data and the predictions obtained by the method of Ceyhan (2012) for DU00-W-212 airfoil at Re=12x10^6. Measured data at Re=3x10^6 is used as the reference point.

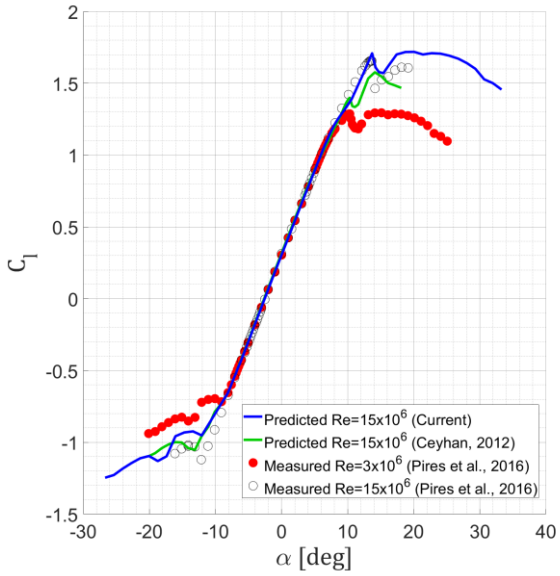

Figure 3.8. Comparison of predicted C_l-α variations with the measured data and the predictions obtained by the method of Ceyhan (2012) for DU00-W-212 airfoil at Re=15x10^6. Measured data at Re=3x10^6 is used as the reference point.

Figures 3.9 and 3.10 present comparisons of predicted C_d-α variations with the experimental data with the predictions obtained using the method proposed by Ceyhan (2012) for Reynolds numbers $6x10^6$ and $9x10^6$, respectively. Generally, $C_{d\,min}$ levels are reasonably well predicted by both methods. The expansion of the drag bucket is better predicted by the current method. However, C_d values are underpredicted in the positive stall region, whereas predicted negative stall C_d values seem to have better agreement with the experimental data.

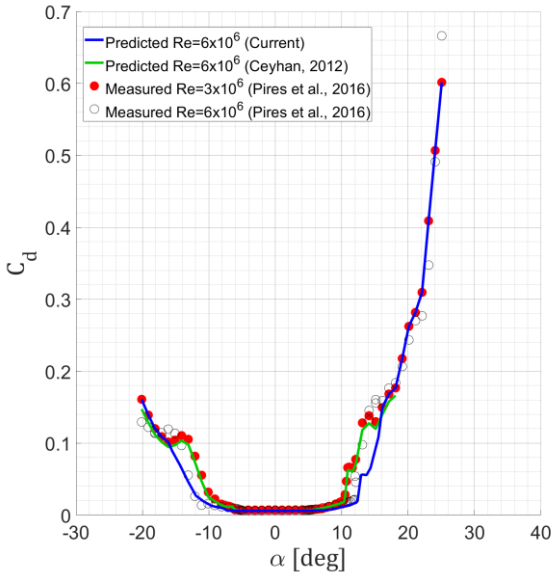

Figure 3.9. Comparison of predicted C_d-α variations with the measured data and the predictions obtained by the method of Ceyhan (2012) for DU00-W-212 airfoil at Re=$6x10^6$. Measured data at Re=$3x10^6$ is used as the reference point.

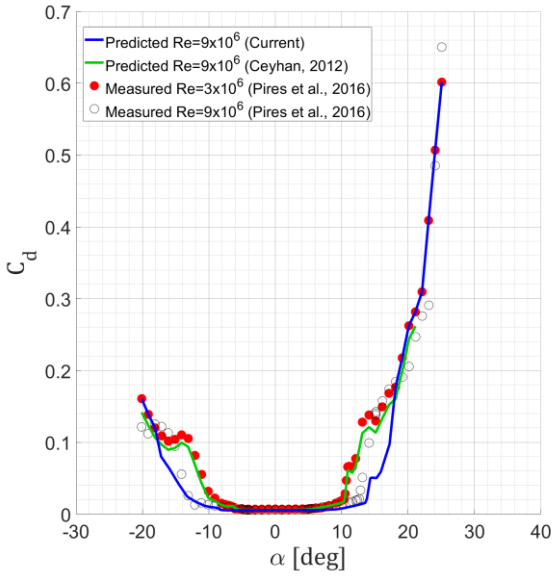

Figure 3.10. Comparison of predicted C_d-α variations with the measured data and the predictions obtained by the method of Ceyhan (2012) for DU00-W-212 airfoil at Re=9x10^6. Measured data at Re=3x10^6 is used as the reference point.

Figures 3.11 and 3.12 show comparisons of predicted C_d-α variations with the experimental data with the predictions obtained using the method proposed by Ceyhan (2012) for Reynolds numbers 12x10^6 and 15x10^6, respectively. Although there is no C_d data in the constructed database for Reynolds numbers that are higher than 9x10^6, the same inferences with the predictions at lower Reynolds numbers can be made here as well. Both methods generally provide accurate predictions for $C_{d\,min}$ levels. The current method performs better in predicting the expansion of the drag bucket. However, the current method tends to underestimate C_d values in the positive stall region, but its predictions around the negative stall region have a better match with the experimental data.

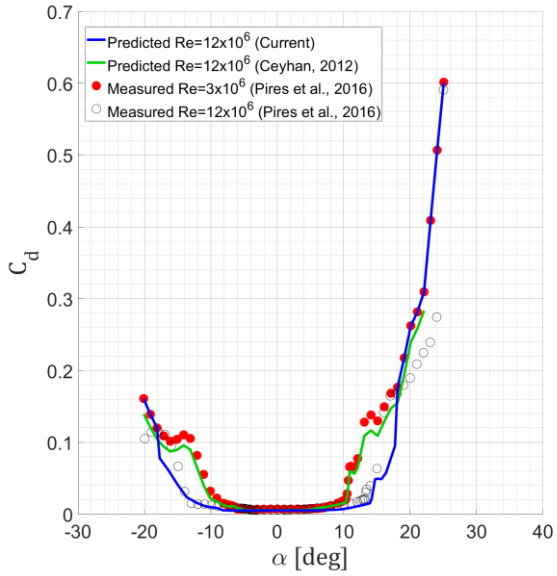

Figure 3.11. Comparison of predicted C_d-α variations with the measured data and the predictions obtained by the method of Ceyhan (2012) for DU00-W-212 airfoil at Re=12x10^6. Measured data at Re=3x10^6 is used as the reference point.

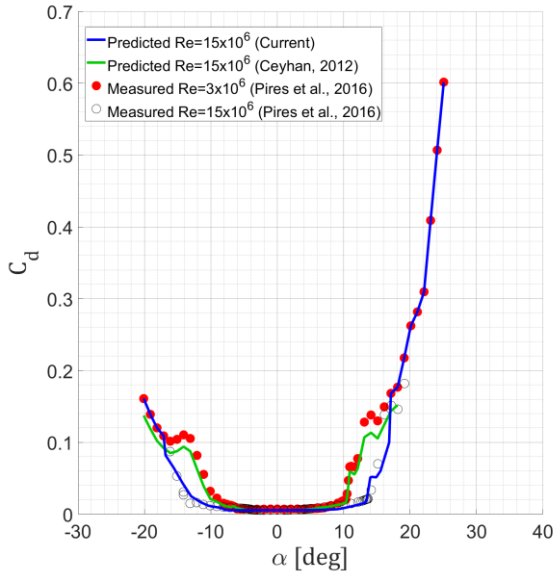

Figure 3.12. Comparison of predicted C_d-α variations with the measured data and the predictions obtained by the method of Ceyhan (2012) for DU00-W-212 airfoil at Re=15x10^6. Measured data at Re=3x10^6 is used as the reference point.

3.2.2 Predictions for NACA $63_{(3)}$018 Airfoil

In this section, the prediction performance for the NACA $63_{(3)}$018 airfoil, which is not included in the constructed database, is represented in detail. Tables 3.8 and 3.9 present a comparison of experimentally measured $C_{l\,max}$ and $C_{d\,min}$ values, respectively, with the predicted ones using the generated response surfaces.

Table 3.8 $C_{l\,max}$ predictions for NACA $63_{(3)}$018 airfoil

Re [x10^{-6}]	$C_{l\,max}$ ***(Experimental)***	$C_{l\,max}$ ***(Predicted)***	***Error [%]***
3	1.25872	1.25332	-0.43
6	1.45304	1.37332	-5.49
9	1.51989	1.44874	-4.68
15	1.63464	1.46584	-10.33
20	1.64279	1.34389	-18.19

Table 3.9 $C_{d\,min}$ predictions for NACA $63_{(3)}$018 airfoil

Re [x10^{-6}]	$C_{d\,min}$ ***(Experimental)***	$C_{d\,min}$ ***(Predicted)***	***Error [%]***
3	0.00584	0.00583	-0.26
6	0.00531	0.00520	-1.99
9	0.00501	0.00501	-0.07
15	0.00479	0.00588	22.77
20	0.00526	0.00790	50.25

For the NACA $63_{(3)}018$ airfoil, $C_{l\,max}$ and $C_{d\,min}$ levels, that are presented in Tables 3.8 and 3.9, are all underpredicted up to Re=$9x10^6$, and the error magnitudes are reasonably acceptable up to this Reynolds number value. For higher Reynolds numbers, the error magnitudes for both coefficients become significantly large. Note that number of symmetric airfoils in the constructed database is only 11 out of 58. This may cause an underrepresentation of symmetric airfoil geometries in terms of their PARSEC parameters in the generated response surfaces, which in turn may be the reason behind these very elevated error levels at these very high Reynolds numbers, which are significantly out-of-range of the database for the NACA $63_{(3)}018$ airfoil.

Table 3.10 shows the calculated n_1 and n_2 coefficients for each extrapolation case. The calculated values are within the ranges proposed by Yamauchi and Johnson up to Re=$9x10^6$. Regarding extrapolating to higher Reynolds number cases, the n values are completely out of these ranges mainly due to the high amount of error levels for $C_{l\,max}$ and $C_{d\,min}$ predictions, as explained above.

Table 3.10 n_1 and n_2 coefficients for extrapolation cases of NACA $63_{(3)}018$ airfoil

Extrapolation Case (Reference Re → Target Re)	$\boldsymbol{n_1}$	$\boldsymbol{n_2}$
3 → 6	0.1257	-0.1663
3 → 9	0.1280	-0.1402
3 → 15	0.0947	0.0043
3 → 20	0.0345	0.1595

Figures 3.13 and 3.14 present comparisons of predicted C_l-α variations with the experimental data with the predictions obtained using the method proposed by Ceyhan (2012) for Reynolds numbers $6x10^6$ and $9x10^6$, respectively. Similar to the

results of the DU00-W-212 airfoil, the change in $C_{l\,max}$ and the corresponding angle of attack values (i.e. stall angle of attack) are underestimated by Ceyhan's method, but the current method predicts these values more successfully. Considering the post-stall predictions, the current method underpredicts the C_l values, unlike the results of the DU00-W-212 airfoil.

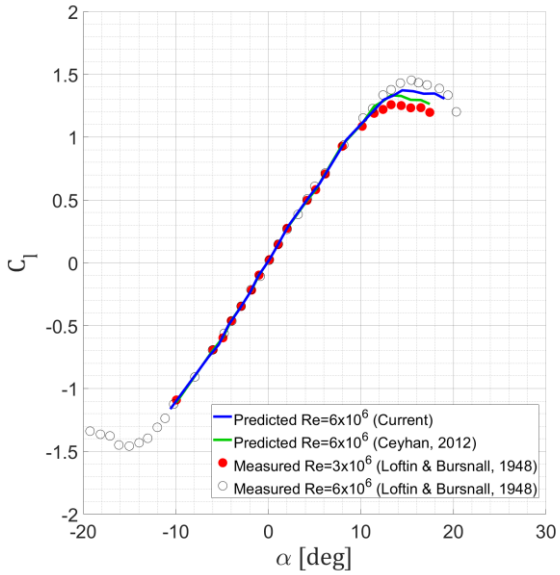

Figure 3.13. Comparison of predicted C_l-α variations with the measured data and the predictions obtained by the method of Ceyhan (2012) for NACA $63_{(3)}018$ airfoil at Re=6x10^6. Measured data at Re=3x10^6 is used as the reference point.

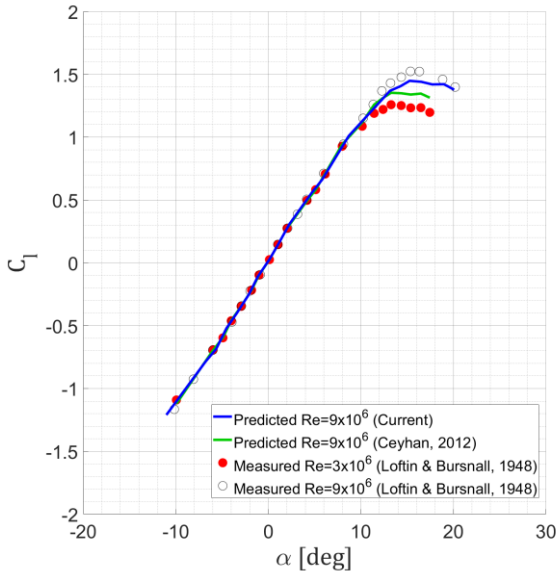

Figure 3.14. Comparison of predicted C_l-α variations with the measured data and the predictions obtained by the method of Ceyhan (2012) for NACA $63_{(3)}018$ airfoil at Re=9x10^6. Measured data at Re=3x10^6 is used as the reference point.

Figures 3.15 and 3.16 present comparisons of predicted C_l-α variations with the experimental data with the predictions obtained using the method proposed by Ceyhan (2012) for Reynolds numbers 15x10^6 and 20x10^6, respectively. The current method fails to predict C_l values around the stall region. This is mainly caused by the highly erroneous predictions for $C_{l\,max}$ value at these Reynolds numbers, as discussed before. In addition, predictions by Ceyhan's method also do not capture the C_l values around this region since the RFOIL simulations cannot predict the increase in C_l values accurately.

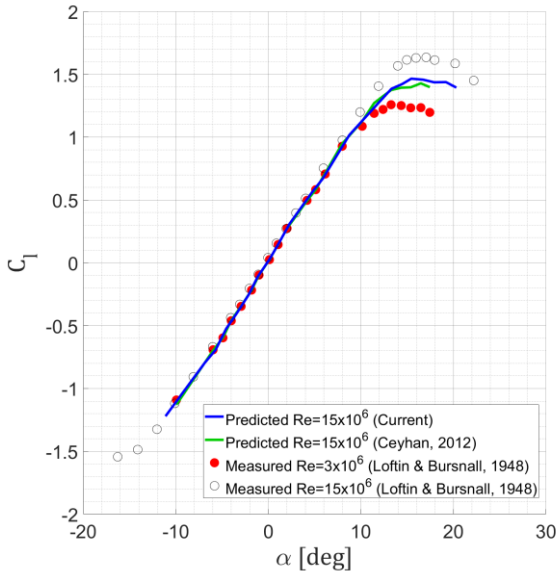

Figure 3.15. Comparison of predicted C_l-α variations with the measured data and the predictions obtained by the method of Ceyhan (2012) for NACA $63_{(3)}$018 airfoil at Re=15x10^6. Measured data at Re=3x10^6 is used as the reference point.

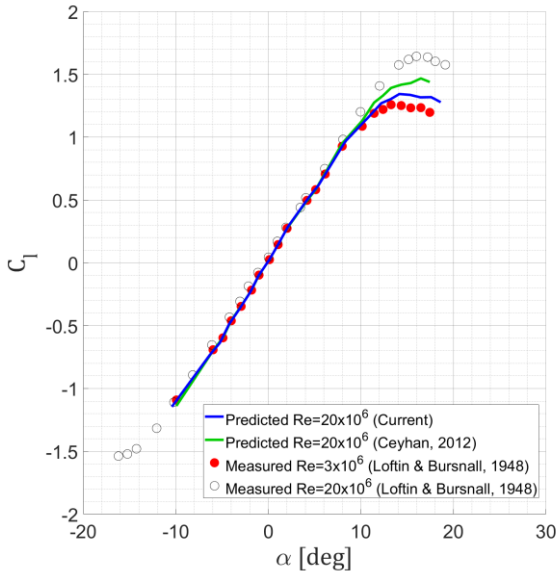

Figure 3.16. Comparison of predicted C_l-α variations with the measured data and the predictions obtained by the method of Ceyhan (2012) for NACA $63_{(3)}$018 airfoil at Re=20x10^6. Measured data at Re=3x10^6 is used as the reference point.

Figures 3.17 and 3.18 illustrate comparisons of predicted C_d-α variations with the experimental data with the predictions obtained using the method proposed by Ceyhan (2012) for Reynolds numbers $6x10^6$ and $9x10^6$, respectively. The decrease in $C_{d\,min}$ levels with increasing Reynolds number is captured well by both methods. Regarding the predictions for the expansion of the drag bucket, it is seen that while the current method slightly overestimates the increase in the size of the expansion, Ceyhan's method underestimates, but predictions by both methods are close to the experimental data at these Reynolds numbers.

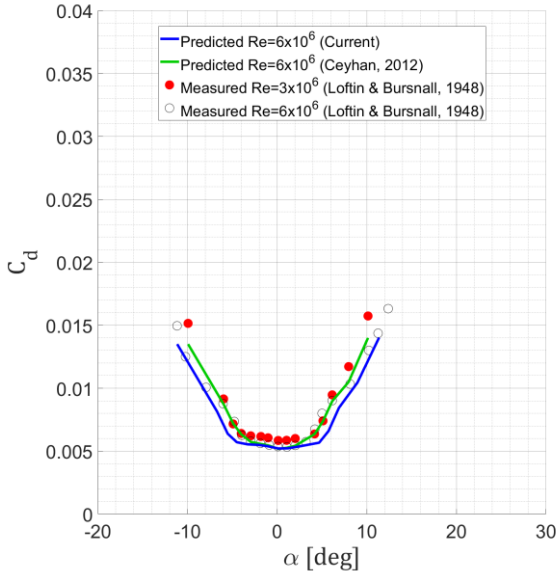

Figure 3.17. Comparison of predicted C_d-α variations with the measured data and the predictions obtained by the method of Ceyhan (2012) for NACA $63_{(3)}018$ airfoil at $Re=6x10^6$. Measured data at $Re=3x10^6$ is used as the reference point.

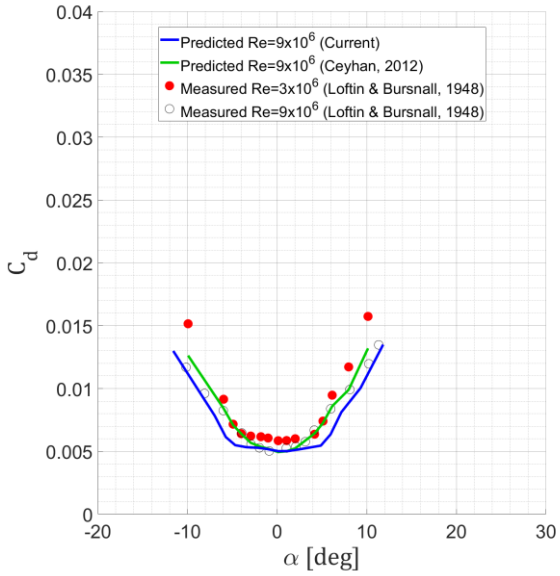

Figure 3.18. Comparison of predicted C_d-α variations with the measured data and the predictions obtained by the method of Ceyhan (2012) for NACA $63_{(3)}$018 airfoil at Re=9x10^6. Measured data at Re=3x10^6 is used as the reference point.

Figures 3.19 and 3.20 illustrate comparisons of predicted C_d-α variations with the experimental data with the predictions obtained using the method proposed by Ceyhan (2012) for Reynolds numbers 15x10^6 and 20x10^6, respectively. Here, Ceyhan's method does a better job of predicting the $C_{d\,min}$ levels as well as the bucket expansion. The current method results in unrealistic predictions at these Reynolds numbers because the power law coefficients, presented in Table 3.10 and discussed the reasons before, are positive, resulting in an increase in C_d values and a decrease in the size of the drag bucket, which is an unexpected outcome with increasing Reynolds number.

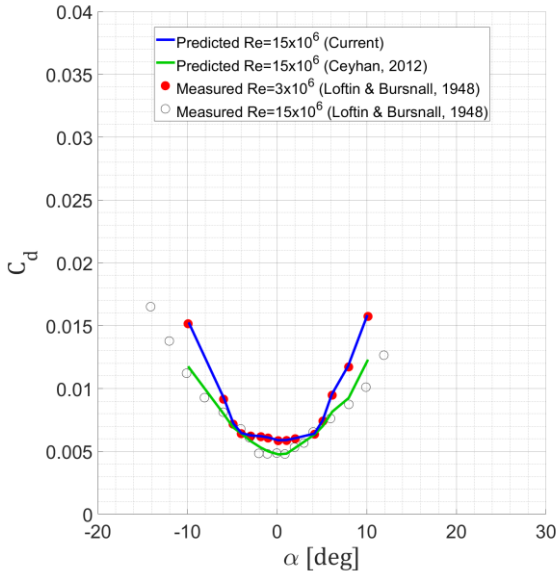

Figure 3.19. Comparison of predicted C_d-α variations with the measured data and the predictions obtained by the method of Ceyhan (2012) for NACA $63_{(3)}$018 airfoil at Re=15x10^6. Measured data at Re=3x10^6 is used as the reference point.

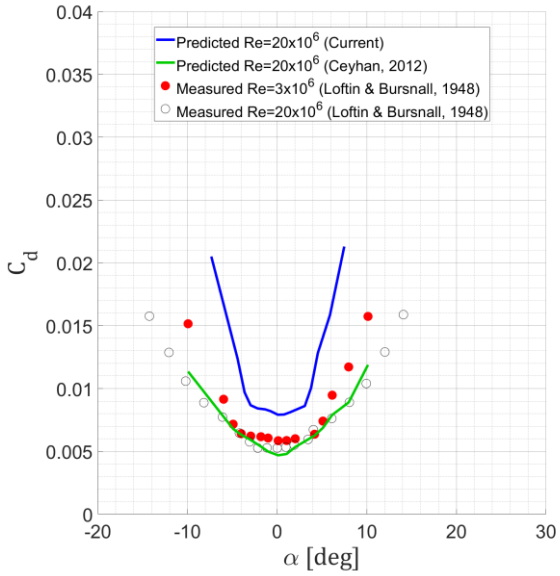

Figure 3.20. Comparison of predicted C_d-α variations with the measured data and the predictions obtained by the method of Ceyhan (2012) for NACA $63_{(3)}$018 airfoil at Re=20x10^6. Measured data at Re=3x10^6 is used as the reference point.

3.3 Sensitivity of the Proposed Method to Reference Reynolds Number

The sensitivity of the proposed method to the reference Reynolds number is examined in this section by making predictions for two different airfoils based on the various reference points. The first airfoil is the DU00-W-212, and predictions are made at the Reynolds number of $12x10^6$, considering the measured data at Reynolds numbers of $3x10^6$, $6x10^6$ and $9x10^6$ as the reference points. The second airfoil is the NREL S825, and predictions are made at $6x10^6$ Reynolds number using the measured data at Reynolds numbers of $1x10^6$, $2x10^6$, $3x10^6$ and $4x10^6$.

A comparison of experimentally measured $C_{l\,max}$ and $C_{d\,min}$ values for DU00-W-212 airfoil was tabulated and discussed in Section 3.2.1. For S825 airfoil, it is represented in Tables 3.11 and 3.12, respectively.

Regarding both $C_{l\,max}$ and $C_{d\,min}$ predictions for the S825 airfoil, error percentages are reasonably low, with the maximum error being about -5.89%. These low error levels are expected since this airfoil is already included in the constructed database. Furthermore, the inclusion of other NREL S-Series airfoils in the database could also play a role in the low error levels.

Table 3.11 $C_{l\,max}$ predictions for S825 airfoil

Re [x10^{-6}]	$C_{l\,max}$ ***(Experimental)***	$C_{l\,max}$ ***(Predicted)***	***Error [%]***
1	1.47218	1.51936	3.21
2	1.55872	1.57069	0.77
3	1.63076	1.61707	-0.84
4	1.68670	1.65849	-1.67
6	1.74503	1.72647	-1.06

Table 3.12 $C_{d\,min}$ predictions for S825 airfoil

Re [x10^{-6}]	$C_{d\,min}$ *(Experimental)*	$C_{d\,min}$ *(Predicted)*	*Error [%]*
1	0.00760	0.00744	-2.09
2	0.00667	0.00687	3.00
3	0.00603	0.00635	5.23
4	0.00590	0.00587	-0.55
6	0.00537	0.00505	-5.89

Using the measured $C_{l\,max}$ and $C_{d\,min}$ values and the predicted ones, the power coefficients are calculated for any extrapolation cases by using Equations 2.13 and 2.14. Table 3.13 shows the calculated n_1 and n_2 coefficients for both airfoils. Then, these coefficients are utilized in the proposed extrapolation method to obtain full lift and drag polars.

Table 3.13 n_1 and n_2 coefficients for any extrapolation cases of DU00-W-212 and S825 airfoil

Airfoil	Extrapolation Case (Reference Re → Target Re)	n_1	n_2
DU00-W-212	3 → 12	0.1868	-0.2172
	6 → 12	0.2011	-0.2145
	9 → 12	0.2607	-0.3082
S825	1 → 6	0.0889	-0.2277
	2 → 6	0.0930	-0.2525
	3 → 6	0.0823	-0.2547
	4 → 6	0.0575	-0.3817

Figure 3.21 represents comparisons of predicted C_l-α variations with the experimentally measured data at $12x10^6$ Reynolds number for the DU00-W-212 airfoil, and Figure 3.22 represents the same comparison at $6x10^6$ Reynolds number for the S825 airfoil. In general, making predictions using different reference Reynolds numbers appears to provide results that are reasonably close to each other. In addition, as seen in the figures, the ability of the proposed method to predict $C_{l\,max}$ does not change with the reference Reynolds number. With regards to the predictions around the post-stall regions, it can be observed that using a reference Reynolds number that is closer to the target Reynolds number is more advantageous since post-stall characteristics become increasingly similar as the reference Reynolds number increases.

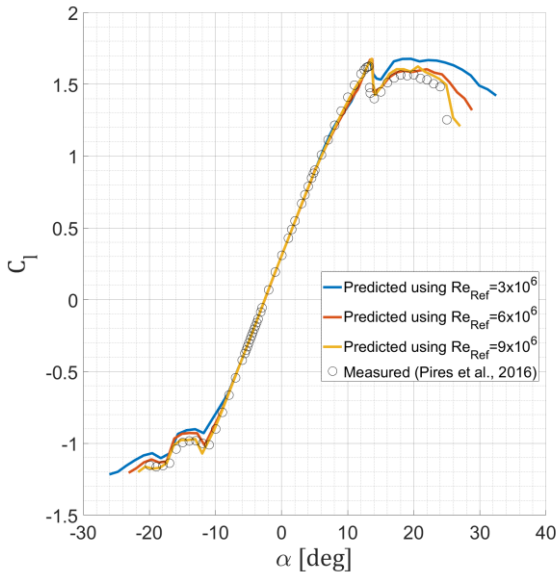

Figure 3.21. Comparison of predicted C_l-α variations with the measured data for DU00-W-212 airfoil at $Re=12x10^6$. Measured data at $Re=3x10^6$, $Re=6x10^6$ and $Re=9x10^6$ are used as the reference points, respectively.

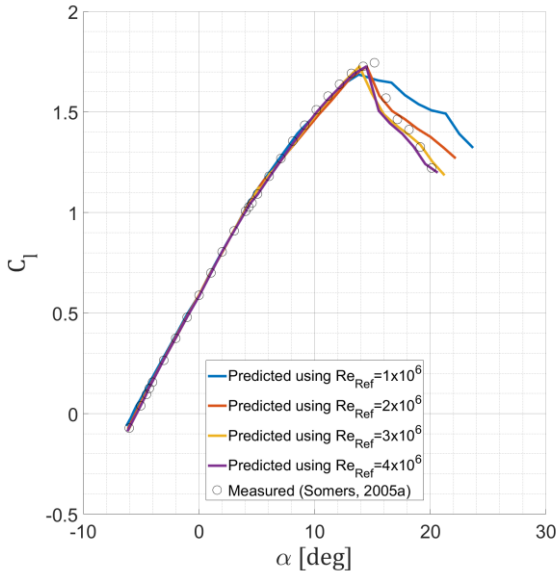

Figure 3.22. Comparison of predicted C_l-α variations with the measured data for S825 airfoil at Re=6x10^6. Measured data at Re=1x10^6, Re=2x10^6, Re=3x10^6 and Re=4x10^6 are used as the reference points, respectively.

Figure 3.23 represents comparisons of predicted C_d-α variations with the experimentally measured data at 12x10^6 Reynolds number for the DU00-W-212 airfoil, and Figure 3.24 represents the same comparison at 6x10^6 Reynolds number for the S825 airfoil. Generally, predictions around $C_{d\,min}$ level seem to be independent of the reference Reynolds number. Furthermore, similar to the C_l-α predictions, using a reference Reynolds number closer to the target value is more powerful for predictions outside the drag bucket since post-stall characteristics become increasingly similar as the reference Reynolds number increases.

As a short summary of this section, utilizing a reference Reynolds number that is closer to the target value provides more accurate predictions for both lift and drag polars. However, conducting wind tunnel test campaigns at high Reynolds numbers can sometimes be challenging, expensive, and time-consuming. In these cases, using the available Reynolds number can still yield acceptable predictions.

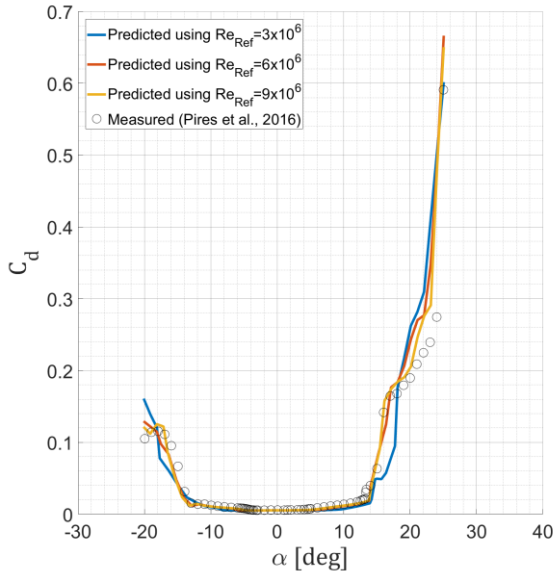

Figure 3.23. Comparison of predicted C_d-α variations with the measured data for DU00-W-212 airfoil at Re=12x10^6. Measured data at Re=3x10^6, Re=6x10^6 and Re=9x10^6 are used as the reference points, respectively.

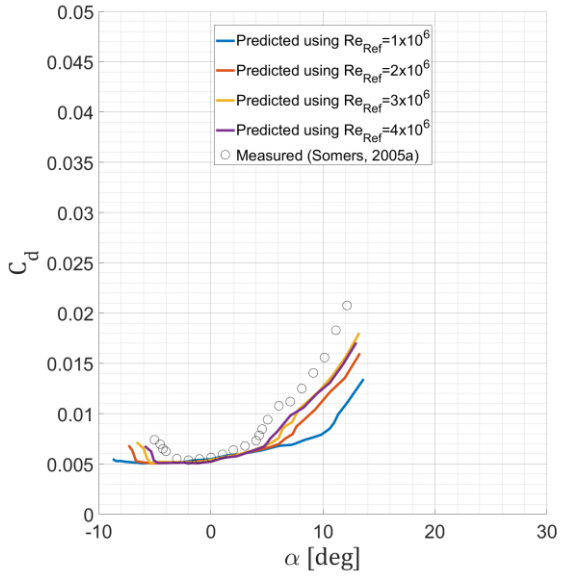

Figure 3.24. Comparison of predicted C_d-α variations with the measured data for S825 airfoil at Re=6x10^6. Measured data at Re=1x10^6, Re=2x10^6, Re=3x10^6 and Re=4x10^6 are used as the reference points, respectively.

CHAPTER 4

AEROELASTIC WIND TURBINE SIMULATIONS

In this chapter, it is aimed to see the effects of predicted polars (using the proposed method) on the operations of a wind turbine by performing aeroelastic BEM simulations. In accordance with this purpose, DTU 10 MW reference wind turbine is selected as a reference since there are lots of sources and works related to it publicly available. HAWC2 software, which is a BEM-based aeroelastic analysis tool, is used to perform simulations because it provides a model for DTU-10MW-RWT as the test case (*HAWC2 Model of DTU 10-MW Reference Wind Turbine*, n.d.).

In the following sections, firstly, the design concept and the specifications of the DTU 10 MW reference wind turbine are explained thoroughly. Secondly, the HAWC2 software environment and its main differences from classical BEM theory are described. Then, the original HAWC2 model for DTU-10MW-RWT is summarized. After that, predicted polars of FFA-W3-241 airfoil, which constitutes one-third of the blades, and its implementation to simulation setup is presented. In the last part, obtained simulation results are presented and compared with the ones existing in the literature.

Figure 4.1. Computer aided drawing of DTU 10 MW reference wind turbine

4.1 DTU 10 MW Reference Wind Turbine

DTU 10 MW reference wind turbine, abbreviated as DTU-10MW-RWT, was developed by the Wind Energy Department of Denmark Technical University (Bak et al., 2013). It is a horizontal axis three-bladed wind turbine with an upwind orientation. Computer-aided drawing of this turbine is shown in Figure 4.1. The General specifications of DTU-10MW-RWT are listed in Table 4.1.

Table 4.1 General specifications of DTU-10 MW-RWT (Bak et al., 2013)

Capacity	10 MW
Orientation and Number of blades	Upwind, 3 blades
Control mechanism	Variable speed and collective pitch
Drivetrain	Medium speed, Multiple stage gearbox
Rotor and Hub diameter	178.3 m, 5.6 m
Hub height	119 m
Cut-in wind speed and rotor speed	4 m/s, 6 RPM
Rated wind speed	11.4 m/s
Cut-out wind speed and rotor speed	25 m/s, 9.6 RPM
Rated tip speed	90 m/s
Pre-cone, Overhang and Shaft tilt	2.5°, 7.07 m, 5°
Rotor mass	229 tons

Figure 4.2 presents the distribution of the chord length, twist and relative thickness along the blade. Blades consist of 5 different airfoil sections, all from the FFA-W3 airfoil family, with thicknesses ranging from 24 to 60%, and one-third of the blades are constituted by the FFA-W3-241 airfoil with 24% thickness. The airfoils utilized in the development of the DTU-10 MW-RWT are displayed in Figure 4.3.

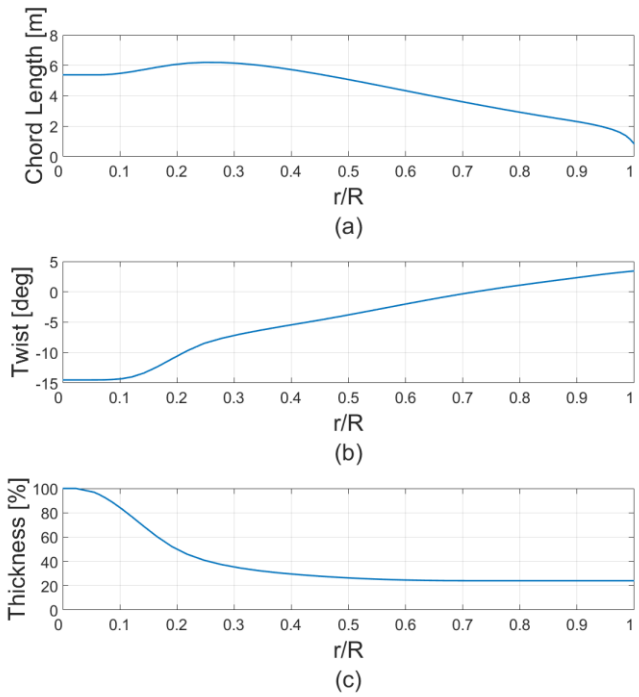

Figure 4.2. (a) Chord, (b) Twist and (c) Thickness distribution along the blade of DTU 10 MW reference wind turbine

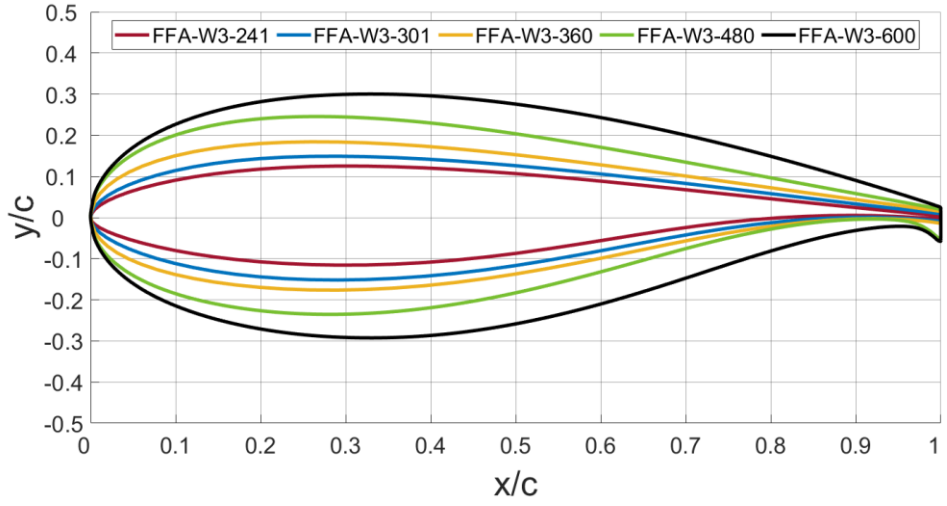

Figure 4.3. The airfoils used in the design of DTU 10 MW reference wind turbine

4.2 HAWC2 Tool

In this study, the HAWC2 code, a BEM-based aeroelastic turbine design tool developed by DTU Wind Energy, was employed (*HAWC2 (Horizontal Axis Wind Turbine Simulation Code 2nd Generation)*, 2003). While high-fidelity CFD calculations are frequently utilized in wind turbine studies, aeroelastic codes such as BEM offer not only computational cost savings but also a satisfactory level of correspondence with CFD results and experimental measurements. Consequently, BEM tools allow for the examination of a broad range of parameters at low costs.

The HAWC2 software includes three modules for simulating the wind, aerodynamics, and structure of a given turbine model under the operations of a controller module during simulations, enabling the simulation of the turbine's operation.

The wind module of HAWC2 consists of two different components, which are the deterministic and stochastic components. The first one is for adjusting the average wind speed with steps and shear, and the second one is for generating the three-dimensional anisotropic turbulent wind flow.

The structural module is built on the turbine's multi-body formulation. In detail, each body, such as the blade, is considered as a Timoshenko beam, and different reference frames are used for each component of the horizontal axis wind turbine, such as the rotor and tower. The connections between the bodies and components are established through algebraic constraints, such as joints, that take into account translation and significant rotation at the connection points.

The module for the aerodynamics of HAWC2 is based on BEM theory with extended features, especially corrections, added to classical BEM to calculate turbine blade loads. Some main corrections and their purposes are summarized and listed in Table 4.2.

Table 4.2 Applied Corrections to classical BEM in HAWC2 software

Correction Name **Method Name** **Reference**	***Correction Purpose***
Tip loss Prandtl (Wilson et al., 1976)	To make calculations for finite number of blades
Non-uniform induction Madsen (Madsen et al., 2012)	To calculate non-uniform induction distribution along the blade elements
Highly loaded rotor Glauert (Glauert, 1935)	To correct problematic predictions at high induction
Dynamic stall Beddoes-Leishmann model (Hansen et al., 2004)	To take into account effect of the fluctuations caused by unsteady inflow and turbulence on blade loads
Dynamic inflow Pitt&Petters (Pitt & Peters, 1977)	To capture effects of instantaneous blade load change on transient rotor wake

4.3 Original HAWC2 Model of DTU-10MW-RWT

As mentioned previously, HAWC2 software provides a model for DTU-10MW-RWT as the test case to perform simulations (*HAWC2 Model of DTU 10-MW Reference Wind Turbine*, n.d.). The aerodynamic polar data embedded in the original model was generated by Bak et al. (2013) and summarized thoroughly in this section.

Bak et al. (2013) generated the aerodynamic polar data of the airfoils by performing 2-dimensional CFD simulations with the free transition for angles of attack in the range from -30 to 30 degrees at certain Reynolds numbers for each airfoil. These Reynolds number values are tabulated in Table 4.3 with respect to airfoils.

Table 4.3 Reynolds number values of performed CFD simulations for all airfoils

Airfoil	***Reynolds Number [10^{-6}]***
FFA-W3-241	12
FFA-W3-301	10
FFA-W3-360	10
FFA-W3-480	10
FFA-W3-600	6

Actually, when conducting BEM simulations, using the aerodynamic polar data at a single Reynolds number for each airfoil section is a rough approximation. Also, it may not accurately capture the full range of aerodynamic behavior of the turbine blades. However, it is a common practice due to the complexity and computational cost of simulating the blade at multiple Reynolds numbers.

The obtained data by performing CFD simulations were corrected using the method proposed by Bak et al. (2006) to take into account the 3-dimensional rotational effects of the turbine, and the resultant data is represented in Figure 4.4. After that,

this polar data was expanded to 360 degrees for outside the normal operating range using the following empirical relations (Zahle et al., 2014):

$$C_l = 2 * \cos(\alpha) * \sin(\alpha) \quad 4.1$$

$$C_d = C_{d\,max} * \sin^2(\alpha) \quad 4.2$$

$$C_m = -\sin(\alpha)/4 \quad 4.3$$

where $C_{d\,max}$ was assumed in the range of 1.5 to 1.3 from the tip to root sections of the blade, at final, obtained data from -180 to +180 degrees angle of attacks is illustrated in Figure 4.5.

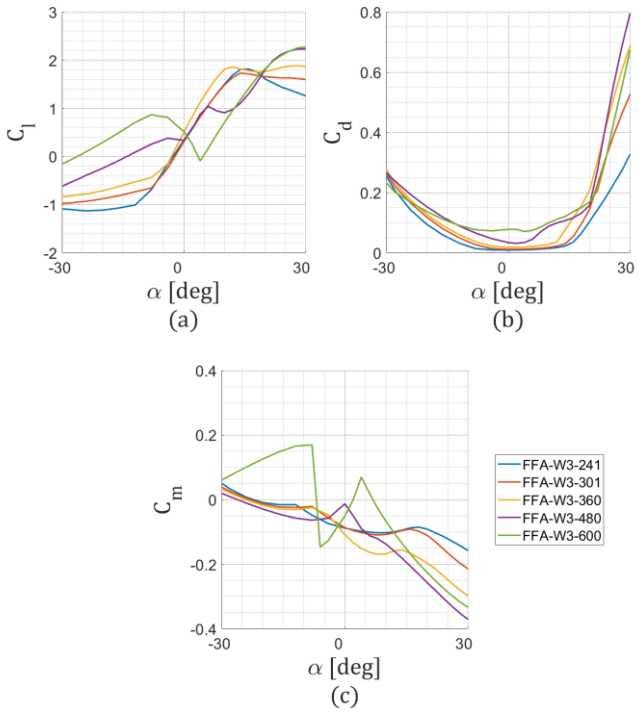

Figure 4.4. 3D corrected (a) lift, (b) drag and (c) moment coefficient vs. angle of attack for FFA-W3-241 airfoil existing in the original HAWC2 model of DTU-10 MW-RWT

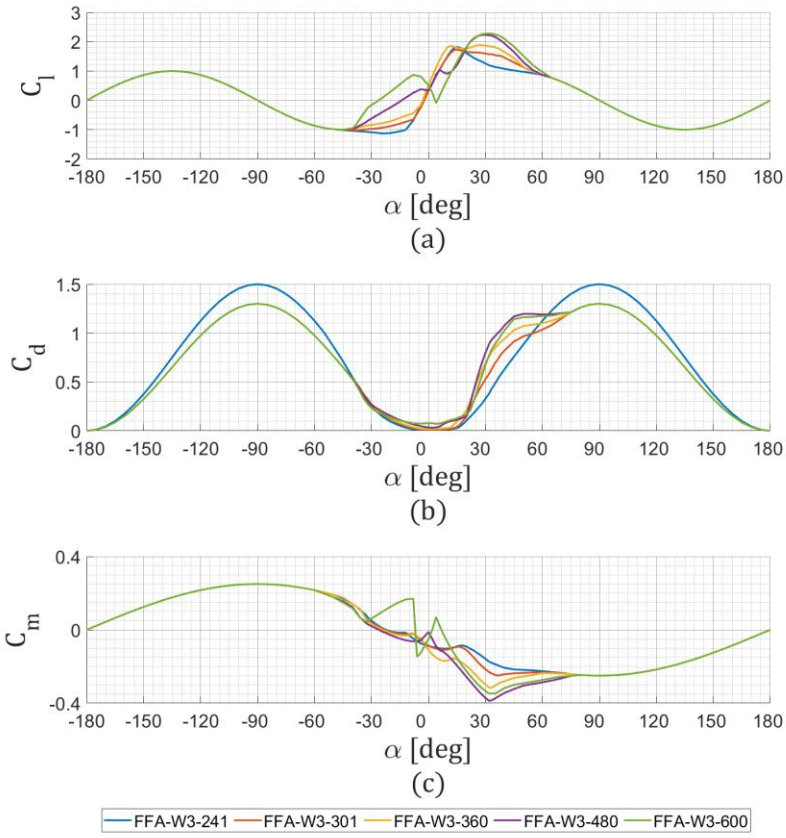

Figure 4.5. (a) Lift, (b) drag and (c) moment coefficient in the range of -180 to 180 degrees angle of attack for FFA-W3-241 airfoil existing in the original HAWC2 model of DTU-10 MW-RWT

4.4 Modifications to Model

In this part, two different cases are created to see the effects of the predicted polars by using the proposed method. In the first case, polar data for the FFA-W3-241 airfoil is predicted at Re=12x10^6 (Polars are also generated at this Reynolds number value in the original model.) by using the proposed method and implemented in aeroelastic simulations. In the second case, instead of using polar data at a single Reynolds number, polar data for the FFA-W3-241 airfoil is generated for 15 different locations on the blade with respect to their local Reynolds number values and implemented in simulations. In the following sub-sections, the generation of the polar data by using the proposed method is presented for both cases.

4.4.1 Case 1

In this section, the polar data for the FFA-W3-241 airfoil is generated at Re=12x10^6 by using the proposed method, and prediction performance is represented. Tables 4.4 and 4.5 show a comparison of CFD predicted (Bak et al., 2013) and experimentally measured $C_{l\,max}$ and $C_{d\,min}$ values, respectively, with the predicted ones using the generated response surfaces.

Table 4.4 $C_{l\,max}$ predictions for FFA-W3-241 airfoil

Re [x10^{-6}]	$C_{l\,max}$ ***(Experimental)***	$C_{l\,max}$ ***(CFD)***	$C_{l\,max}$ ***(Predicted)***	***Difference [%]***
1.6	1.3742	N/A	1.3747	0.03
12	N/A	1.8665	1.8015	-3.48

Table 4.5 $C_{d\,min}$ predictions for FFA-W3-241 airfoil

Re [x10^{-6}]	$C_{d\,min}$ ***(Experimental)***	$C_{d\,min}$ ***(CFD)***	$C_{d\,min}$ ***(Predicted)***	***Difference [%]***
1.6	0.00969	N/A	0.00975	0.63
12	N/A	0,00919	0.00694	-24.48

Regarding the predicted $C_{l\,max}$ and $C_{d\,min}$ values by corresponding response surfaces at 1.6x10^6 Reynolds number, the difference level from the experimental measurement is really low. The reason behind it is that the FFA-W3-241 airfoil and its measured data at 1.6x10^6 is included in the constructed database.

Since there is not any measurement at 12x10^6 in the open literature, predicted values are compared with the CFD predictions. For $C_{l\,max}$, prediction by the response surface is slightly low compared to the CFD prediction. In contrast, predicted $C_{d\,min}$ is significantly lower than the CFD prediction.

After that, n_1 and n_2 are calculated to extrapolate measured lift and drag polar at 1.6x10^6 to 12x10^6. The calculated power coefficients are tabulated in Table 4.6.

Table 4.6 n_1 and n_2 coefficients for extrapolation case of FFA-W3-241 airfoil

Extrapolation Case (Reference Re → Target Re)	n_1	n_2
1.6 → 12	0,1342	-0,1683

These power law coefficients are utilized in the proposed extrapolation method, and the obtained full lift and drag polars are compared with CFD predictions in Figures

4.6 and 4.7, respectively. Regarding the C_l estimations, both predictions generally have an agreement with each other up to the stall point. The predicted $C_{l\,max}$ values by the current method is slightly less than the CFD predicted ones. Regarding the C_d estimations, it is observed that predictions by the current method are underestimated compared to the CFD predicted ones.

These predicted lift and drag polars by the current method are combined at the same angle of attacks; then changed with the polar data of the original model within the predicted angle of attack range to perform aeroelastic BEM simulations of Case 1. The simulation results are given in Section 4.5.

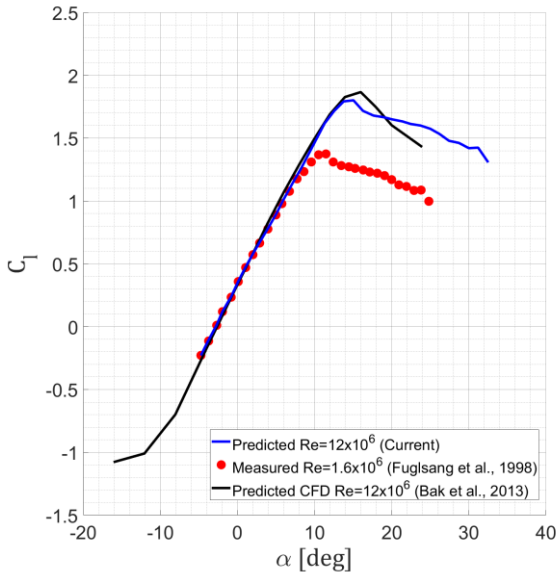

Figure 4.6. Comparison of predicted C_l-α variation with the predicted CFD data for FFA-W3-241 airfoil at Re=12x10^6. Measured data at Re=1.6x10^6 is used as the reference point.

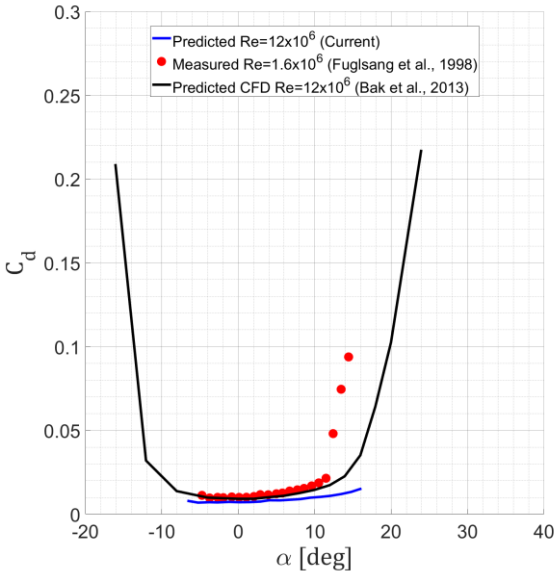

Figure 4.7. Comparison of predicted C_d-α variation with the predicted CFD data for FFA-W3-241 airfoil at Re=12x10^6. Measured data at Re=1.6x10^6 is used as the reference point.

4.4.2 Case 2

In this section, the polar data generation for the FFA-W3-241 airfoil is presented for 15 different locations on the blade (60.8, 63.7, 66.5, 69.2, 71.7, 74.0, 76.2, 78.2, 80.0, 81.6, 83.0, 84.2, 85.1, 85.7 and 86.4 meters away from the root) with respect to their local Reynolds number values.

The local Reynolds number values for these 15 different locations on the blade are obtained by simulating the original model with wind speeds ranging from 4 to 25 m/s at intervals of 1 m/s. Figure 4.8 illustrates the obtained Reynolds number distributions along the entire blade for wind speeds of 5, 10, 15, 20 and 25 m/s. As seen in the figure, the Reynolds number in locations formed from the FFA-W3-241 airfoil varies approximately between 3x10^6 and 17x10^6.

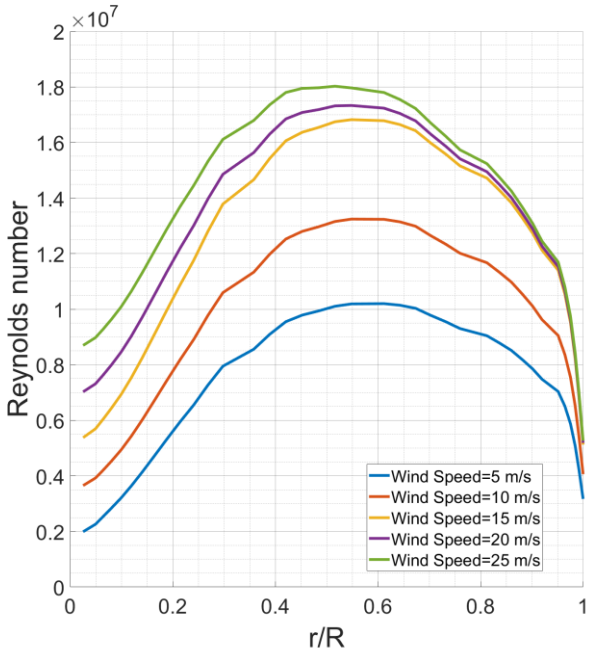

Figure 4.8. The obtained Reynolds number distributions along the blade at wind speeds of 5, 10, 15, 20 and 25 m/s by simulating the original model

After obtaining local Reynolds number values, lift and drag polar data are generated using the proposed method for the FFA-W3-241 airfoil at 15 different sections for all wind speed cases from 4 to 25 m/s (at intervals of 1 m/s). Considering all combinations of the sections and the wind speed cases, 330 different lift and drag polar data are predicted. As an example, predicted lift and drag polar data for the sections along the blade at the wind speed of 10 m/s are shown in Figures 4.9 and 4.10, respectively.

All these predicted lift and drag polars by the current method for each wind speed value are combined at the same angle of attacks; then changed with the polar data of the original model within the predicted angle of attack range to perform aeroelastic BEM simulation of Case 2. The simulation results are given in Section 4.5.

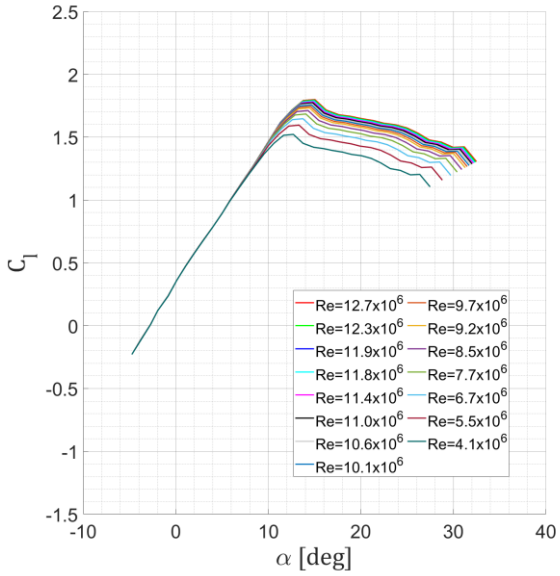

Figure 4.9. The C_l-α variations with respect to local Reynolds number values predicted by the proposed method for 15 different sections formed by the FFA-W3-241 airfoil along the blade at wind speed of 10 m/s

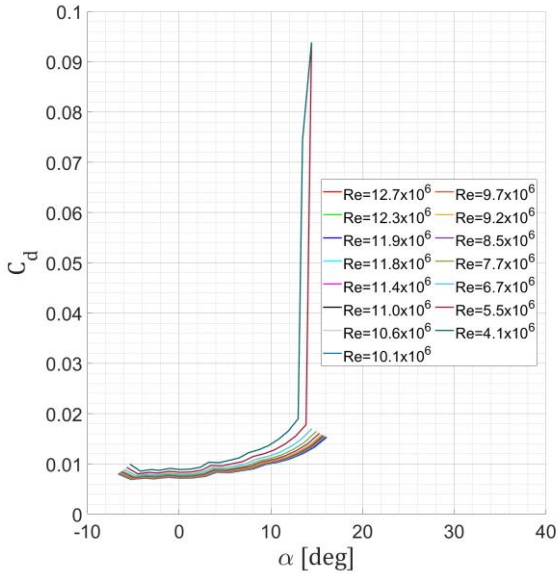

Figure 4.10. The C_d-α variations with respect to local Reynolds number values predicted by the proposed method for 15 different sections formed by the FFA-W3-241 airfoil along the blade at wind speed of 10 m/s

4.5 Aeroelastic Simulation Results

In this section, aeroelastic BEM simulation results of the original model, Case 1 and Case 2, described in Sections 4.3 and 4.4, are presented. Simulations are carried out for wind speeds ranging from 4 to 25 meters per second (from cut-in to cut-out wind speed) for all three cases. Operational conditions for pitch angle and rotational speed controlled by the basic DTU Wind Energy controller are summarized in Table 4.7 with respect to wind speed.

Table 4.7 Operational conditions of aeroelastic BEM simulations

Wind speed [m/s]	***Pitch [deg]***	***RPM***
4.0	2.681	6.000
5.0	1.896	6.000
6.0	0.863	6.000
7.0	0.000	6.000
8.0	0.000	6.149
9.0	0.000	6.912
10.0	0.000	7.671
11.0	0.000	8.423
12.0	3.717	9.600
16.0	11.588	9.600
20.0	16.614	9.600
25.0	21.901	9.600

Tables 4.8 and 4.9 represent the comparison of the generated power and thrust values by the turbine obtained from the simulation results of the original model, Case 1 and Case 2.

Regarding the power results presented in Table 4.8, estimated power values in Case 1 and Case 2 are almost the same at all wind speeds. In addition, estimated power values in the original model are also very close to these levels for all wind speeds.

Table 4.8 Comparison of the Generated Power Values for the Original Model, Case 1 and Case 2

Wind speed [m/s]	***Original Model*** ***Power [kW]***	***Case 1*** ***Power [kW]***	***Case 2*** ***Power [kW]***
5.0	824.1	858.7	855.2
6.0	1565.7	1592.3	1583.9
8.0	3706.6	3725.2	3713.9
9.0	5266.4	5291.8	5286.0
10.0	7200.1	7233.4	7233.3
11.0	9538.6	9581.0	9585.4
12.0	10682.2	10681.8	10681.8
16.0	10678.5	10678.6	10678.5
20.0	10680.4	10680.6	10680.6

The estimated thrust values shown in Table 4.9 are similar to the power results in that they show little difference between Case 1 and Case 2 at all wind speeds. Additionally, the estimated power values in the original model also align with these levels for all wind speeds.

Table 4.9 Comparison of the Generated Thrust Values for the Original Model, Case 1 and Case 2

Wind speed [m/s]	***Original Model*** ***Thrust [kN]***	***Case 1*** ***Thrust [kN]***	***Case 2*** ***Thrust [kN]***
5.0	339.2	335.9	335.7
6.0	484.6	472.2	472.0
8.0	749.9	732.3	730.5
9.0	945.1	922.9	921.7
10.0	1160.1	1132.8	1132.2
11.0	1393.2	1360.5	1360.3
12.0	1276.4	1254.4	1258.7
16.0	831.0	819.5	819.4
20.0	675.7	664.9	665.6

Figure 4.11 shows the operational angle of attack values obtained from the simulation results of the original model for the 15 different sections formed by the FFA-W3-241 airfoil on the blade with respect to wind speeds of 5, 10, 15, 20 and 25 m/s. As seen in the figure, the range of the operational angle of attack values varies approximately from -4 to 8 degrees. Remembering the generated polars for Case 1 and Case 2 in Sections 4.4.1 and 4.4.2, it can be said that lift and drag coefficient values in the angle of attack range from -4 to 8 degrees remain almost unchanged within this range. This explains the minimal differences in the estimated generated power and thrust values between the original model and modified cases.

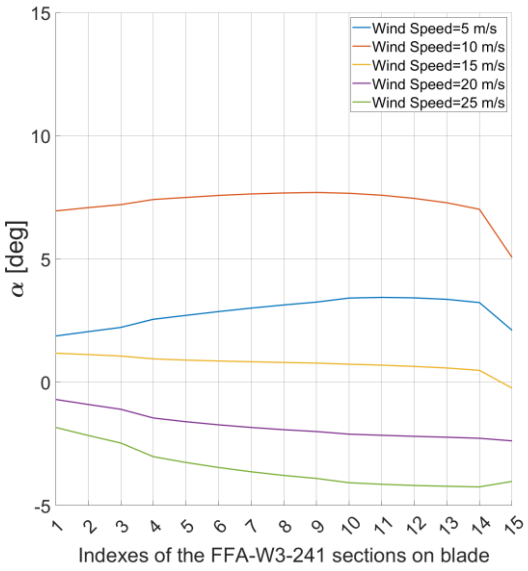

Figure 4.11. The operational angle of attack values for the 15 different sections formed by the FFA-W3-241 airfoil on the blade

Figures 4.12 and 4.13 represent the variations of the estimated mechanical thrust and power values with respect to the wind speed for the original model, Case 1 and Case 2. Regarding the obtained mechanical power values, estimations by both modified cases seem almost the same as the estimations by the original model at any wind speed cases. This is because lift polar is the dominant polar in the power term, and predicted polars are very close to polars generated by Bak et al. (2013) since the operational angle of attack values is within the linear region of the lift polar. In addition, the thrust estimations by both modified cases have good agreement with the estimations by the original model. It is seen that there are only minimal differences between the estimations caused by the minimal differences between the predicted drag polars and polar generated by Bak et al. (2013) within the operational angle of attack range.

Consequently, it is deduced that performed aeroelastic simulation results using predicted polars by the proposed method are consistent with the simulation results of the original model using CFD predicted polars. This can be considered an

advantage for the proposed method because it is a more economical way compared to performing CFD simulations to generate data at higher Reynolds number values.

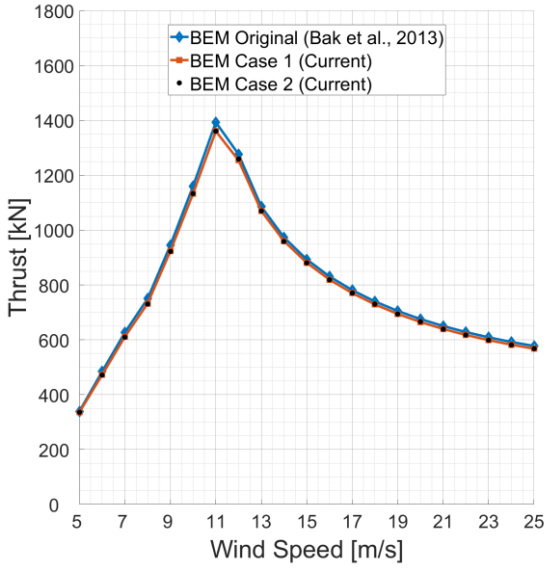

Figure 4.12. Comparison of Predicted Generated Mechanical Power Values for all cases

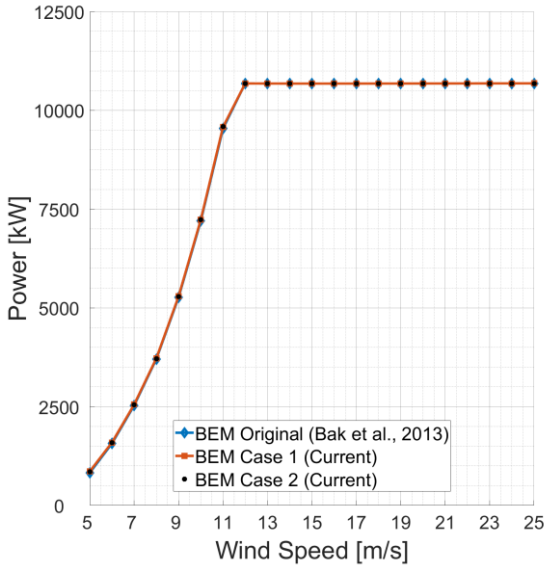

Figure 4.13. Comparison of Predicted Generated Mechanical Thrust Values for all cases

CHAPTER 5

CONCLUSIONS

5.1 Concluding Remarks

In this thesis study, a data-driven approach that utilizes a power law to extrapolate the Reynolds number is proposed, and its impact on the aerodynamic polars of wind turbine airfoils is investigated. For this purpose, a database is constructed with experimentally obtained aerodynamic data from the open literature for airfoils with a thickness-to-chord ratio (t/c) of 15% to 30%, which is more applicable to wind turbine blade design. All airfoils in the database are parameterized using the PARSEC airfoil parameterization method to enhance the database in terms of geometric properties. Pareto analysis is then performed to understand the sensitivity of the maximum lift coefficient ($C_{l\,max}$) and minimum drag coefficient ($C_{d\,min}$) to PARSEC geometric properties and the Reynolds number using JMP statistical software. Based on this analysis, response surfaces are generated to predict $C_{l\,max}$ and $C_{d\,min}$ for a given airfoil operating at a given Reynolds number. These predicted values are utilized in a proposed power law based estimation method to obtain predictions for the full polars.

The efficacy of this proposed Reynolds number extrapolation method is evaluated by making predictions for airfoils that are both present and absent in the database in order to understand the influence of being included in the database. The results show that the response surfaces generated through the current data-driven approach, as well as the full polar prediction methodology show better agreement with experimental results compared to the numerical simulations-based extrapolations scheme. For airfoil types that might be underrepresented in the database, the prediction results can be erroneous, especially at very high Reynolds numbers that are not in the constructed database.

Subsequent to that, the predicted polars for the FFA-W3-241 airfoils are integrated into aeroelastic BEM simulations to examine the impact on the operations of the DTU 10 MW reference wind turbine. The simulation results using the predicted polars by the current method seem to be consistent with results from the literature within the operational range of the angle of attack values. This can be considered an advantage for the current method because it is a more economical way compared to performing CFD simulations to generate data at higher Reynolds number values.

5.2 Future Work

In the future, the constructed airfoil database can be enhanced with the increasing available experimental data in the open literature. This will enable more accurate predictions for various airfoil types at much higher Reynolds numbers. Furthermore, the airfoil database can be augmented by including thinner airfoils, and the proposed methodology can be extended to use for other aeronautical applications. In addition, a similar database can be constructed from the CFD simulation results of many kinds of airfoils, and predictions at higher Reynolds numbers can be obtained without the need for additional CFD simulations.

REFERENCES

Abbott, I. H., von Doenhoff, A. E., & Stivers, L. S. (1945). *NACA Report No. 824 - Summary of Airfoil Data*.

Akram, M. T., & Kim, M.-H. (2021). Aerodynamic Shape Optimization of NREL S809 Airfoil for Wind Turbine Blades Using Reynolds-Averaged Navier Stokes Model—Part II. *Applied Sciences*, *11*(5). https://doi.org/10.3390/app11052211

Bak, C., Johansen, J., & Andersen, P. B. (2006). Three-Dimensional Corrections of Airfoil Characteristics Based on Pressure Distributions. *European Wind Energy Conference, 2006*. https://www.researchgate.net/publication/237435464

Bak, C., Zahle, F., Bitsche, R., Kim, T., Yde, A., Christian Henriksen, L., Nata-rajan, A., & Hartvig Hansen, M. (2013). *Department of Wind Energy I-Report Description of the DTU 10 MW Reference Wind Turbine*.

Bellini, F., Bonfanti, N., Chieti, S., & Civati, M. (2017). *CB2: Airfoil Optimization with GUI*. MATLAB Central File Exchange. https://www.mathworks.com/matlabcentral/fileexchange/65251-cb2-airfoil-optimization-with-gui

Bertagnolio, F. ;, Sørensen, N. N. ;, Johansen, J. ;, & Fuglsang, P. (2001). *Wind Turbine Airfoil Catalogue*.

Ceyhan, Ö. (2012). *Towards 20MW Wind Turbine: High Reynolds Number Effects on Rotor Design*. https://doi.org/https://doi.org/10.2514/6.2012-1157

Fuglsang, P., Antoniou, I., Dahl, K. S., & Madsen, H. Aa. (1998). *Wind Tunnel Tests of the FFA-W3-241, FFA-W3-301 and NACA 63-430 Airfoils*. Riso National Laboratory.

Ge, M., Tian, D., & Deng, Y. (2014). *Reynolds Number Effect on the Optimization of a Wind Turbine Blade for Maximum Aerodynamic Efficiency*. https://doi.org/10.1061/(ASCE)EY.1943-7897

Glauert, H. (1935). Airplane Propellers. In *Aerodynamic Theory: A General Review of Progress Under a Grant of the Guggenheim Fund for the Promotion of Aeronautics* (pp. 169–360). Springer Berlin Heidelberg. https://doi.org/10.1007/978-3-642-91487-4_3

Global Wind Report 2022. (2022).

Hansen, M. H., Gaunaa, M., & Aagaard Madsen, H. (2004). *A Beddoes-Leishman type dynamic stall model in state-space and indicial formulations* (Issue 1354(EN)).

Hartman, L. (2022, August 16). *Wind Turbines: the Bigger, the Better*. https://www.energy.gov/eere/articles/wind-turbines-bigger-better

HAWC2 (Horizontal Axis Wind turbine simulation Code 2nd generation). (2003). DTU Wind Energy. https://www.hawc2.dk/

HAWC2 model of DTU 10-MW Reference Wind Turbine. (n.d.). Retrieved December 11, 2022, from https://www.hawc2.dk/download/hawc2-model/dtu-10-mw-reference-wind-turbine

Jacobs, E. N., & Sherman, A. (1939). *Airfoil Section Characteristics as Affected by Variations of the Reynolds Number*.

JMP (No. 12). (2015). SAS Institute Inc.

Kappanman, R. F. (1971). A Note on the Multivariate t-ratio Distribution. *The Annals of Mathematical Statistics, 42*(1), 349–351.

Khuri, A. I., & Mukhopadhyay, S. (2010). Response Surface Methodology. In *Wiley Interdisciplinary Reviews: Computational Statistics* (Vol. 2, Issue 2, pp. 128–149). https://doi.org/10.1002/wics.73

Llorente, E., Gorostidi, A., Jacobs, M., Timmer, W. A., Munduate, X., & Pires, O. (2014). Wind Tunnel Tests of Wind Turbine Airfoils at High Reynolds Numbers. *Journal of Physics: Conference Series*, *524*(1). https://doi.org/10.1088/1742-6596/524/1/012012

Loftin, L. K., & Bursnall, W. J. (1948). *NACA-TN-1773 The Effects of Variations in Reynolds Number Between 3.0 x 10 to the Power 6 and 25.0 x 10 to the Power 6 upon the Aerodynamic Characteristics of a Number of NACA 6-series Airfoil Sections*.

Madsen, H. A., Riziotis, V., Zahle, F., Hansen, M. O. L., Snel, H., Grasso, F., Larsen, T. J., Politis, E., & Rasmussen, F. (2012). Blade element momentum modeling of inflow with shear in comparison with advanced model results. *Wind Energy*, *15*(1), 63–81. https://doi.org/10.1002/we.493

Mccroskey, W. J. (1987). *A Critical Assessment of Wind Tunnel Results for the NACA 0012 Airfoil*.

Pettersson, K., & Rizzi, A. (2008). Aerodynamic scaling to free flight conditions: Past and present. *Progress in Aerospace Sciences*, *44*(4), 295–313. https://doi.org/10.1016/j.paerosci.2008.03.002

Pfanzagl, J., & Sheynin, O. (1996). Studies in the history of probability and statistics XLIV A forerunner of the t-distribution. *Biometrika*, *83*(4), 891–898.

Pires, O., Munduate, X., Ceyhan, O., Jacobs, M., & Snel, H. (2016). Analysis of high Reynolds numbers effects on a wind turbine airfoil using 2D wind tunnel test data. *Journal of Physics: Conference Series*, *753*(2). https://doi.org/10.1088/1742-6596/753/2/022047

Pitt, D. M., & Peters, D. A. (1977, September). Rotor Dynamic Inflow Derivatives and Time Constants from Various Inflow Models. *9th European Rotorcraft Forum*.

Sobieczky, H. (1997). *New Design Concepts for High Speed Air Transport*. https://doi.org/10.1007/978-3-7091-2658-5

Somers, D. M. (1997a). *Design and Experimental Results for the S809 Airfoil*.

Somers, D. M. (1997b). *Design and Experimental Results for the S814 Airfoil*.

Somers, D. M. (2005a). *Design and Experimental Results for the S825 Airfoil*.

Somers, D. M. (2005b). *Design and Experimental Results for the S827 Airfoil*.

Sommers, D. M., & Tangler, J. L. (2000, June). *Wind-Tunnel Tests of Two Airfoils for Wind Turbines Operating at High Reynolds Numbers*. http://www.doe.gov/bridge

Timmer, W. A., & van Rooij, R. P. J. O. M. (2003). Summary of the Delft University Wind Turbine Dedicated Airfoils. *AIAA-2003-0352*. https://doi.org/https://doi.org/10.2514/6.2003-352

van Dam, C. P. (2009). *Blade Aerodynamics - Passive and Active Load Control for Wind Turbine Blades*.

van Rooij, R. P. J. O. M., & Timmer, W. A. (2003). Roughness Sensitivity Considerations for Thick Rotor Blade Airfoils. *Journal of Solar Energy Engineering, Transactions of the ASME*, *125*(4), 468–478. https://doi.org/10.1115/1.1624614

Wallmann, S., & Klein, C. (2010). Investigation of High Reynolds Number Effects on Rotor Blades for Wind Turbines. *European Wind Energy Conference and Exhibition*.

Wilson, R. E., Lissaman, P. B. S., & Walker, S. N. (1976). *Aerodynamic performance of wind turbines. Final report*. https://doi.org/https://doi.org/10.2172/7315651

Wiser, R., Bolinger, M., Hoen, B., Millstein, D., Rand, J., Barbose, G., Darghouth, N., Gorman, W., Jeong, S., & Paulos, B. (2022). *Land-Based Wind Market Report: 2022 Edition*. http://www.osti.gov

Yamauchi, G. K., & Johnson, W. (1983). *Trends of Reynolds Number Effects on Two-Dimensional Airfoil Characteristics for Helicopter Rotor Analyses*. https://ntrs.nasa.gov/search.jsp?R=19830016201

Zahle, F., Bak, C., Guntur, S., Sørensen, N. N., & Troldborg, N. (2014). Comprehensive aerodynamic analysis of a 10 MW wind turbine rotor using 3D CFD. *32nd ASME Wind Energy Symposium*. https://doi.org/10.2514/6.2014-0359

APPENDICES

A. Names of the 47 NACA airfoils mentioned in Part 2.1

Table A.1 Names of the 47 NACA airfoils mentioned in Part 2.1

NACA 2418	NACA $63_{(3)}418$	NACA $64_{(4)}021$	NACA $65_{(4)}421$
NACA 2421	NACA $63_{(3)}618$	NACA $64_{(4)}221$	NACA $65_{(215)}114$
NACA 2424	NACA $63_{(4)}021$	NACA $64_{(4)}421$	NACA $65(_{421)}420$
NACA 4415	NACA $63_{(4)}221$	NACA $65_{(2)}015$	NACA $66_{(2)}015$
NACA 4418	NACA $63_{(4)}421$	NACA $65_{(2)}215$	NACA $66_{(2)}215$
NACA 4421	NACA $64_{(2)}015$	NACA $65_{(2)}415$	NACA $66_{(2)}415$
NACA 4424	NACA $64_{(2)}215$	NACA $65_{(3)}018$	NACA $66_{(3)}018$
NACA $63_{(2)}015$	NACA $64_{(2)}415$	NACA $65_{(3)}218$	NACA $66_{(3)}218$
NACA $63_{(2)}215$	NACA $64_{(3)}018$	NACA $65_{(3)}418$	NACA $66_{(3)}418$
NACA $63_{(2)}415$	NACA $64_{(3)}218$	NACA $65_{(3)}618$	NACA $66_{(4)}021$
NACA $63_{(2)}615$	NACA $64_{(3)}418$	NACA $65_{(4)}021$	NACA $66_{(4)}221$
NACA $63_{(3)}218$	NACA $64_{(3)}618$	NACA $65_{(4)}221$	

B. Response Surface Equation to Predict $C_{l\,max}$

Response surface equation to predict $C_{l\,max}$ is written below. Reynolds number should be used by dividing $1x10^6$ in this equation.

$$
\begin{aligned}
C_{l\,max} = {} & 7.09865 + 0.04039\,x\,Re + -82.13060\,x\,p_2 \\
& - 18.52819\,x\,p_3 + 5.53977\,x\,p_5 \\
& - 36.12375\,x\,p_7 - 1.67344\,x\,p_8 \\
& + 0.08227\,x\,p_{11} + Re\,x\,(Re\,x - 0.00248) \\
& + Re\,x\,(p_2\,x - 0.78798) + p_2\,x\,(p_2\,x \\
& - 747.47463) + Re\,x\,(p_3\,x - 0.05545) \\
& + p_2\,x\,(p_3\,x\,55.69473) \\
& + p_3\,x\,(p_3\,x\,10.36978) + Re\,x\,(p_5\,x \\
& - 0.05392) + p_2\,x\,(p_5\,x - 48.39435) \\
& + p_3\,x\,(p_5\,x - 12.98456) \\
& + p_5\,x\,(p_5\,x\,0.59853) + Re\,x\,(p_7\,x \\
& - 0.06285) + p_2\,x\,(p_7\,x - 884.52420) \\
& + p_3\,x\,(p_7\,x - 0.08802) + p_5\,x\,(p_7\,x \\
& - 51.17662) + p_7\,x\,(p_7\,x - 75.94095) \\
& + Re\,x\,(p_8\,x\,0.00376) + p_2\,x\,(p_8\,x \\
& - 21.60166) + p_3\,x\,(p_8\,x - 1.25134) \\
& + p_5\,x\,(p_8\,x - 3.32374) \\
& + p_7\,x\,(p_8\,x\,2.09291) + p_8\,x\,(p_8\,x \\
& - 0.03983) + Re\,x\,(p_{11}\,x - 0.00076) \\
& + p_2\,x\,(p_{11}\,x - 0.29001) + p_3\,x\,(p_{11}\,x \\
& - 0.03848) + p_5\,x\,(p_{11}\,x\,0.08406) \\
& + p_7\,x\,(p_{11}\,x - 0.49156) + p_8\,x\,(p_{11}\,x \\
& - 0.01246) + p_{11}\,x\,(p_{11}\,x - 0.00035)
\end{aligned}
$$

C. Response Surface Equation to Predict $C_{d\,min}$

Response surface equation to predict $C_{d\,min}$ is written below. Reynolds number should be used by dividing $1x10^6$ in this equation.

$$
\begin{aligned}
C_{d\,min} = {} & 0.01575 + 0.00010 \text{ x Re} + 0.21373 \text{ x } p_1 \\
& - 0.31378 \text{ x } p_2 - 0.12073 \text{ x } p_3 \\
& - 0.02787 \text{ x } p_4 + 0.08197 \text{ x } p_6 \\
& + 0.00025 \text{ x } p_8 + \text{Re x (Re x } 0.00002) \\
& + \text{Re x } (p_1 \text{ x } - 0.00088) \\
& + p_1 \text{ x } (p_1 \text{ x } 3.46256) + \text{Re x } (p_2 \text{ x} \\
& - 0.00038) + p_1 \text{ x } (p_2 \text{ x } - 1.73228) \\
& + p_2 \text{ x } (p_2 \text{ x } 5.64787) + \text{Re x } (p_3 \text{ x} \\
& - 0.00150) + p_1 \text{ x } (p_3 \text{ x } 1.15585) \\
& + p_2 \text{ x } (p_3 \text{ x } 2.16899) + p_3 \text{ x } (p_3 \text{ x } 0.28212) \\
& + \text{Re x } (p_4 \text{ x } 0.00077) + p_1 \text{ x } (p_4 \text{ x} \\
& - 6.81224) + p_2 \text{ x } (p_4 \text{ x } - 0.70536) \\
& + p_3 \text{ x } (p_4 \text{ x } - 0.49835) \\
& + p_4 \text{ x } (p_4 \text{ x } 1.73978) \\
& + \text{Re x } (p_6 \text{ x } 0.00044) + p_1 \text{ x } (p_6 \text{ x} \\
& - 0.60758) + p_2 \text{ x } (p_6 \text{ x } - 1.21056) \\
& + p_3 \text{ x } (p_6 \text{ x } - 0.22306) \\
& + p_4 \text{ x } (p_6 \text{ x } 0.09239) + p_6 \text{ x } (p_6 \text{ x } 0.00244) \\
& + \text{Re x } (p_8 \text{ x } - 0.00024) \\
& + p_1 \text{ x } (p_8 \text{ x } 0.23765) + p_2 \text{ x } (p_8 \text{ x} \\
& - 0.13786) + p_3 \text{ x } (p_8 \text{ x } - 0.01190) \\
& + p_4 \text{ x } (p_8 \text{ x } - 0.03526) \\
& + p_6 \text{ x } (p_8 \text{ x } 0.01369) + p_8 \text{ x } (p_8 \text{ x } 0.00098)
\end{aligned}
$$